UNIVERSIDADE FEDERAL FLUMINENSE

INSTITUTO DE GEOCIÊNCIAS

DEPARTAMENTO DE GEOLOGIA E GEOFÍSICA

PROGRAMA DE PÓS-GRADUAÇÃO EM DINÂMICAS DOS OCEANOS E DA TERRA

MATHEUS NILO DE OLIVEIRA

DEEP LEARNING-BASED APPLICATIONS TO SEISMIC FAULT SEGMENTATION IN BRAZILIAN PRE-SALT

Niterói, RJ

2025

MATHEUS NILO DE OLIVEIRA

DEEP LEARNING-BASED APPLICATIONS TO SEISMIC FAULT SEGMENTATION IN BRAZILIAN PRE-SALT

Dissertation submitted to the Programa de Pós-Graduação em Dinâmica dos Oceanos e da Terra of Universidade Federal Fluminense in partial fulfillment of the requirements for the degree of Master Geology and Geophysics.

Advisor: PhD. Wagner Moreira Lupinacci

Co-advisor: PhD. Eberton Rodrigues de Oliveira Neto

Niterói, RJ

2025

Ficha catalográfica automática - SDC/BIG
Gerada com informações fornecidas pelo autor

D278d De Oliveira, Matheus Nilo
Deep learning-based applications to seismic fault segmentation in brazilian pre-salt : Deep learning-based applications to seismic fault segmentation in brazilian pre-salt / Matheus Nilo De Oliveira. - 2025.
78 f.: il.

Orientador: Wagner Moreira Lupinacci.
Coorientador: Eberton Rodrigues De Oliveira Neto.
Dissertação (mestrado)-Universidade Federal Fluminense, Instituto de Geociências, Niterói, 2025.

1. Seismic Fault Segmentation. 2. Deep Learning. 3. Automatic Fault Identification. 4. Produção intelectual. I. Lupinacci, Wagner Moreira, orientador. II. De Oliveira Neto, Eberton Rodrigues, coorientador. III. Universidade Federal Fluminense. Instituto de Geociências. IV. Título.

CDD - XXX

Bibliotecário responsável: Debora do Nascimento - CRB7/6368

DEEP LEARNING-BASED APPLICATIONS TO SEISMIC FAULT SEGMENTATION IN BRAZILIAN PRE-SALT

MATHEUS NILO DE OLIVEIRA

Dissertation submitted to the Programa de Pós-Graduação em Dinâmica dos Oceanos e da Terra of Universidade Federal Fluminense in partial fulfillment of the requirements for the degree of Master in Geology and Geophysics.

Approved by the Committee on 28/01/1997

Committee:

____

Ph. D. Ana Claudia Veronese Aguiar Krueger (BLUWARE)

____

Ph. D. Alexsandro Guerra Cerqueira (GAIA/INCT-GP/UFBA)

____

Ph. D. João Paulo Rodrigues Zambrini (ASPENTECH)

____

Ph. D. Eberton Rodrigues de Oliveira Neto – Co-advisor (Petrobras)

____

Ph.D. Wagner Moreira Lupinacci – Advisor (GIECAR/GGO/UFF and INCT-GP)

Niterói, RJ

2025

"Entrai pela porta estreita, porque larga é a porta da perdição e espaçoso o caminho que a ela conduz, e muitos são os que por ela entram."

(S. Mateus, 7:13 e 14.)

Evangelho Segundo o Espiritismo

Acknowledgments

Agradeço imensamente a presença de Deus na minha vida e toda instrução que a mim foi dada ao longo dos anos através dos seus mensageiros. Adorei as almas, mãe Maria, vós que cuidaste do teu filho e acompanha cada passo, orientando e o reerguendo. Oni Ibejada, com a alegria das palmas que trazem consigo eu agradeço pela sabedoria e cuidado. Okê arô, Sultão das Matas, obrigado por abrir os meus caminhos depositando a energia dos caboclos na minha vida. Laroyê, seu Lalu, por acompanhar a minha jornada e abrir meus caminhos. A Umbanda é paz e amor!

Aos meus pais, Keu e Vilson, por todo amor, carinho, suporte e orientação. Dona Keu é a minha maior incentivadora e minha melhor amiga. É um privilégio poder vivenciar essa jornada ao seu lado e mais privilégio ainda poder dizer que seremos Mestres! Cada passo, cada desafio e cada obstáculo, conquistamos juntos, então nada mais justo que esse título seja seu também. Seu Vilson é um exemplo de que podemos alcançar nossos objetivos independente de idade, só precisamos ter fé e dedicação. Vocês dois são exemplos de “heróis da vida real”.

A Wagner Lupinacci eu agradeço pelas oportunidades, confiança e orientação. Acolheu o meu jeito “baiano demais” para o grupo e abriu os caminhos no laboratório depositando fé na minha capacidade e me incentivando a me aprimorar cada vez mais. Ao professional e pesquisador que venho me tornando, você tem grande influência. E esse é só o começo!

A Tone Rodrigues, Eberton, Eberto, Everton, Tony, Toni, dentre outros fragmentados, meus sinceros agradecimentos. Não só pela orientação nem por todo trabalho produzido em parceria, mas pela amizade e companheirismo. Você é um cara singular e certamente foi um grande presente da vida ser seu amigo.

A Fabio Júnior (não, não é o cantor), obrigado! Largar família e amigos e viver um desafio em outra cidade não é algo fácil e sua amizade tornou o processo mais tranquilo. Voce é ponto fora da curva e tem minha admiração tanto pela sua amizade quanto pelo seu talento. Planejaremos muitas trilhas juntos ainda!

A Gabriela Marinho, pela amizade que sempre que nosso grupo estiver reunidos, certamente sairão boas risadas. Ligadíssima no 220V que ao escrever isso já imagino voce lendo com estardalhaço.

Ao meu cheiro preferido, Paula Luiza, eu agradeço! Você chegou como uma surpresa pra preencher o que eu precisava. Sou muito abençoado de poder vivenciar o amor ao seu lado e dividir a jornada. Obrigado por me fazer sentir o calor no coração e me mostrar que nosso romance é como "neve na praia".

A todo o grupo do GIECAR, obrigado pelos momentos de cafezinho, resenha, perturbação e muito apoio moral e técnico!

Aos membros da banca, agradeço o tempo dedicado a ler essa dissertação e avaliação.

Agradeço à Petrobras pelo financiamento do projeto de pesquisa e desenvolvimento, ao INCT-GP pelo suporte à pesquisa e à ANP pelo fornecimento dos dados.

É isto, pessoal, vamos pra próxima etapa! O céu é o limite…

Abstract

This dissertation explores the application of deep learning techniques to seismic fault segmentation, focusing on carbonate reservoirs in the Brazilian pre-salt. In naturally fractured reservoirs, faults and fractures can enhance permeability, which is essential for optimizing production strategies. However, they also pose challenges during drilling, as they may create instability zones or modify pore pressure, increasing the risk of wellbore collapse or blowouts. I investigate the use of deep learning-based applications, especially convolutional neural networks, to improve fault interpretation in Brazilian pre-salt. A synthetic dataset was generated using a robust workflow that applies point-spread function (PSF) convolution to simulate the broadband seismic characteristics of pre-salt fields. This dataset was carefully designed to replicate the geological challenges of pre-salt reservoirs, ensuring realistic training conditions for CNN. Seismic data preconditioning was employed to enhance data quality, incorporating edge-preserving smoothing filters guided by fault probability attributes to reduce noise and artifacts while preserving geological detail. The CNN achieved high accuracy in detecting faults with varying displacements, significantly outperforming traditional geometric attribute methods, especially in resolving subtle and complex fault structures.

Keywords: deep learning, Brazilian pre-salt, seismic fault, automatic seismic fault interpretation, Buzios field, seismic synthetic data, convolutional neural networks, seismic fault detection, machine learning, seismic data preconditioning.

Resumo

Esta dissertação explora a aplicação de técnicas de aprendizado profundo para segmentação sísmica de falhas, com foco em reservatórios carbonáticos do pré-sal brasileiro. Em reservatórios naturalmente fraturados, falhas e fraturas podem aumentar a permeabilidade, o que é essencial para otimizar estratégias de produção. No entanto, elas também apresentam desafios durante a perfuração, pois podem criar zonas de instabilidade ou aumento de pressão de poros, elevando o risco de colapsos de poço. Investigo o uso de aplicações baseadas em aprendizado profundo, especialmente redes neurais convolucionais (CNNs), para aprimorar a interpretação de falhas no pré-sal brasileiro. Um conjunto de dados sintético foi gerado utilizando um fluxo de trabalho robusto que aplica a convolução da função de espalhamento de ponto (PSF) para simular as características sísmicas de banda larga dos campos do pré-sal. Esse conjunto de dados foi cuidadosamente projetado para replicar os desafios geológicos associados aos reservatórios do pré-sal, garantindo condições realistas de treinamento para a CNN. O pré-condicionamento dos dados sísmicos foi empregado para melhorar a qualidade dos dados, incorporando filtros de suavização que preservam bordas, guiados por atributos de probabilidade de falhas, com o objetivo de reduzir ruídos e artefatos, ao mesmo tempo em que preservam os detalhes geológicos. A CNN demonstrou alta precisão na detecção de falhas com deslocamentos variados, superando significativamente os métodos tradicionais baseados em atributos geométricos, especialmente na resolução de estruturas de falhas sutis e complexas.

Palavras-chave: aprendizado profundo, pré-sal brasileiro, falha sísmica, interpretação automática de falhas, campo de Búzios, dados sísmicos sintéticos, redes neurais convolucionais, detecção de falha sísmica, aprendizado de máquina, pré-condicionamento de dado sísmico.

List of Figures

Summary

1. Seismic fault characterization

1.1. Brazilian pre-salt: a brief introduction

Carbonate reservoirs represent around 60% of the petroleum reserves of the world (Chopra et al., 2005) and have a crucial role in the world energetic scenario. From the second half of the year 2000, the carbonate reservoirs in Brazil became of great interest due to the discovery of presalt plays.

The Santos Basin is the largest offshore basin and extends from the southern coast of the State of Rio de Janeiro to the northern part of the State of Santa Catarina, between the 230th and 280th parallels of latitude south, in the southeastern region of the Brazilian continental margin. Bordered to the north by the Cabo Frio high (which separates it from the Campos Basin) and to the south by the Florianópolis high (which separates it from the Pelotas Basin), the Santos Basin covers an area of approximately 350,000 km² up to a bathymetric height of 3,000 m. This area is almost three times the size of the Campos Basin. Figure 1 shows the location of the Santos Basin.

The first exploratory well in the pre-salt section of the Santos Basin was drilled in 2006 to evaluate the Parati Prospect. Although this well discovered only gas and condensate that was commercially unattractive, it proved the existence of an active petroleum system in that part of the basin, indicating the existence of a new exploratory play in the Santos Basin: the pre-salt play (Petersohn, 2013). In 2006, the discovery of Tupi prospect in the deepwater section was also announced. Discovered with oil accumulation in Neoaptian carbonate reservoirs, the Tupi prospect would become the first commercial discovery in the pre-salt of the Santos Basin. By the end of 2010, the Tupi prospect was declared commercially viable and was subsequently renamed the Lula Field.

In 2010, the year in which the federal government sanctioned the new regulatory framework for pre-salt areas, wells 2-ANP-1-RJS (Franco) and 2-ANP-2-RJS (Libra) were drilled, finding huge oil reserves (Petersohn, 2013).

Since Petrobras announced its discovery in 2007, the pre-salt has stood out as the largest oil reserve in the world in the last 50 years. These reserves consist of large deposits of light oil, highly valuable on the market. Furthermore, it is notable for its significant productivity. As of February 2022, approximately 75% of Brazil's total oil and natural gas production came from pre-salt, with 75% of this volume coming from the Santos Basin.

The economic importance of the presalt carbonate reservoirs is matched by the exploration challenges posed by these rocks. Carbonates are highly complex rocks associated with reservoirs that are difficult to characterize, produce and manage. Therefore, more studies are needed to fully understand the unique characteristics of these deposits, as their properties can vary significantly from one field to another.Wright and Barnett (2015) proposed a division of the carbonate reservoir in the pre-salt section based on the intra-Alagoan unconformity. They identified two types of "microbial" limestone: one from the rift phase, which is located between the pre-Alagoan and intra-Alagoan unconformities, and another from the Sag phase, which is situated above the intra-Alagoan unconformity and extends to the base of the salt layer. These correspond to the coquinas of the Itapema Formation and the limestone of the Barra Velha Formation, both commonly referred to as "microbial." Initially, coquinas were regarded as secondary carbonate reservoirs (Formigli, 2009). However, with the discovery of large accumulations in the Mero and Buzios fields, they have become increasingly significant targets for exploration in the pre-salt section of the Santos Basin (Kattah, 2015).

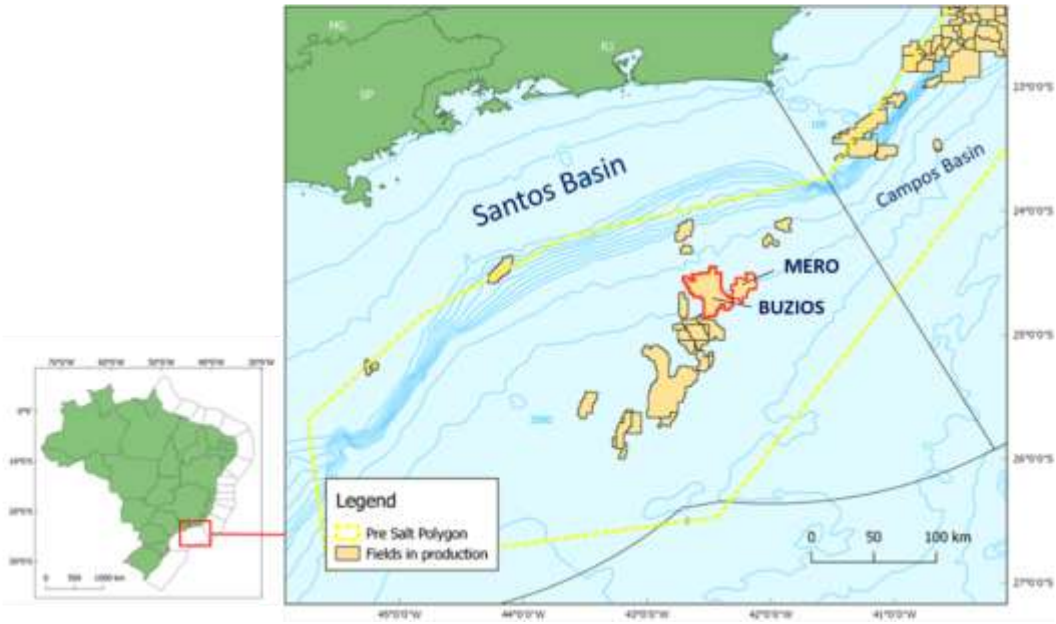

Figure 1 - Map location of the Búzios and Mero fields and Santos Basin.

The main challenge for the study area is the imaging of highly fractured carbonate reservoirs with variable thickness situated in ultra-deep water and underlain in highly convoluted stratified layers of salt..

1.2. Role of faults in carbonate reservoir characterization

Mapping faults and fractures in pre-salt reservoirs is crucial due to their significant influence on hydrocarbon exploration, reservoir management, and production efficiency. Naturally fractured carbonate reservoirs are a major source of global hydrocarbons, hosting some of the largest and most productive fields (Chopra and Marfurt, 2005; Ding et al., 2020). Faults and fractures often serve as pathways or barriers for hydrocarbon migration, playing a critical role in forming structural traps that enable oil and gas accumulation. Understanding their geometry helps predict the movement and distribution of hydrocarbons within the reservoir (Golsanami et al., 2020). Additionally, these features impact reservoir connectivity, which is vital for determining how fluids flow between compartments and for forecasting reservoir performance.

In the context of Brazilian pre-salt, Mendes et al. (2022) highlight the importance of a detailed topological characterization of fault networks. They stress that understanding the connectivity and orientation of faults is essential for optimizing hydrocarbon extraction in pre-salt reservoirs. It also demonstrates how a thorough analysis of fault systems can improve the reliability of reservoir models and enhance predictions of fluid flow dynamics. This, in turn, contributes to more effective resource management in complex geological environments.

Libra carbonate reservoirs are marked by substantial heterogeneity, which is further compounded by the presence of igneous rock formations.. This complexity presents challenges for both reservoir modeling and predicting production performance. Zhao et al. (2019) examine the genetic causes of magma events and their relationship with fault activity, thereby enhancing the reliability and accuracy of predictions regarding igneous rock distributions within the reservoir.

Hughes and Darby (2021) analyze the Santos Basin, focusing on faults, carbonate deposition, and lake level changes and demonstrate that this approach optimizes pre-salt asset development by reducing uncertainty in lateral variability and exposure surface distribution.

Seismic attributes, such as semblance and curvature, are essential for interpreting geological structures like faults and folds. Common attributes for fault and fracture detection in seismic data include coherence, fault likelihood, and gradient structure tensor (Bhattachary and Verma, 2019). Recently, convolutional neural networks (CNNs) have gained popularity for fault detection in image segmentation, where faults are labeled as ones and non-faults as zeros (Guo et al., 2020; An et al., 2021).

1.3. Conventional methods: seismic attributes

1.3.1. Coherence

The application of seismic coherence attributes has transformed the processes of fault identification and mapping within subsurface geological formations. Bahorich and Farmer (1995) introduced the coherence cube technique, representing a significant advancement in the visualization of subsurface discontinuities. Their approach highlighted the effectiveness of coherence in detecting faults and stratigraphic features that could be missed using traditional amplitude-based methods..

Coherence attributes measures the similarity between seismic traces, employing values from 0 to 1 to indicate the degree of similarity. A coherence value of 0 suggests discontinuity, while a value of 1 indicates continuity. Common methods for calculating coherence include cross-correlation of seismic traces and semblance analysis. Marfurt et al. (1998) developed a semblance-based technique to detect structural and stratigraphic discontinuities, such as faults. Semblance measures the consistency of seismic traces within a specified window, quantifying how similar the traces are to an average trace. This approach, sensitive to lateral changes in amplitude, has proven useful for detecting subtle geological features.

The semblance coherence is defined as the ratio of the energy of the mean trace to the total energy within a group of traces, offering a quantitative measure of seismic trace similarity:

$$C_{semb} = \frac{ME_a}{E} \tag{1}$$

where E_a is the energy of the average trace, and E is the total energy.

The similarity attribute, as described by Tingdahl et al. (2001), quantifies the Euclidean distance between seismic trace vectors, providing a measure of trace similarity based on their amplitude and shape. High similarity values indicate closely related traces, whereas low values suggest greater dissimilarity. This method can be sensitive to amplitude variations, especially in low-frequency bandwidths and in data with low signal-to-noise ratios.

Understanding and applying coherence attributes significantly enhance seismic data interpretation. By highlighting discontinuities and subtle changes in seismic reflections, geoscientists can better delineate structural features and stratigraphic variations. This plays a pivotal role in hydrocarbon exploration, aiding in the identification of potential reservoirs and refining geological models for more accurate predictions.

Marfurt et al. (1998) applied coherence attributes to three-dimensional seismic data, refining the ability to detect and map intricate fault networks. Their methodology utilized semblance-based calculations to identify structural and stratigraphic discontinuities with greater accuracy. By emphasizing lateral changes in seismic responses, they enhanced the interpreter's ability to delineate fault planes and fracture systems essential for reservoir characterization.

Further advancements were made by Chopra and Marfurt (2007), who integrated coherence attributes with a range of other seismic attributes, providing a more holistic view of the subsurface. They emphasized the importance of combining coherence with curvature and other geometric attributes to enhance the visualization of fault structures and subtle stratigraphic features.

In a different approach, Tingdahl and de Groot (2003) explored the use of dip-steering techniques in conjunction with coherence attributes to improve the detection of dipping reflectors. By accounting for local dip variations, they mitigated the misinterpretation of inclined geological features as discontinuities. This refinement allowed for more accurate mapping of faults in areas with complex tectonics.

Recently, Qi et al. (2017) utilized coherence attributes alongside advanced imaging technologies to map faults within unconventional shale reservoirs. They used an image processing-based fault detection method involving fault enhancement and skeletonization that processes coherence data to output fault probability and compared it to a U-Net architecture to fault detection (Figure 2).

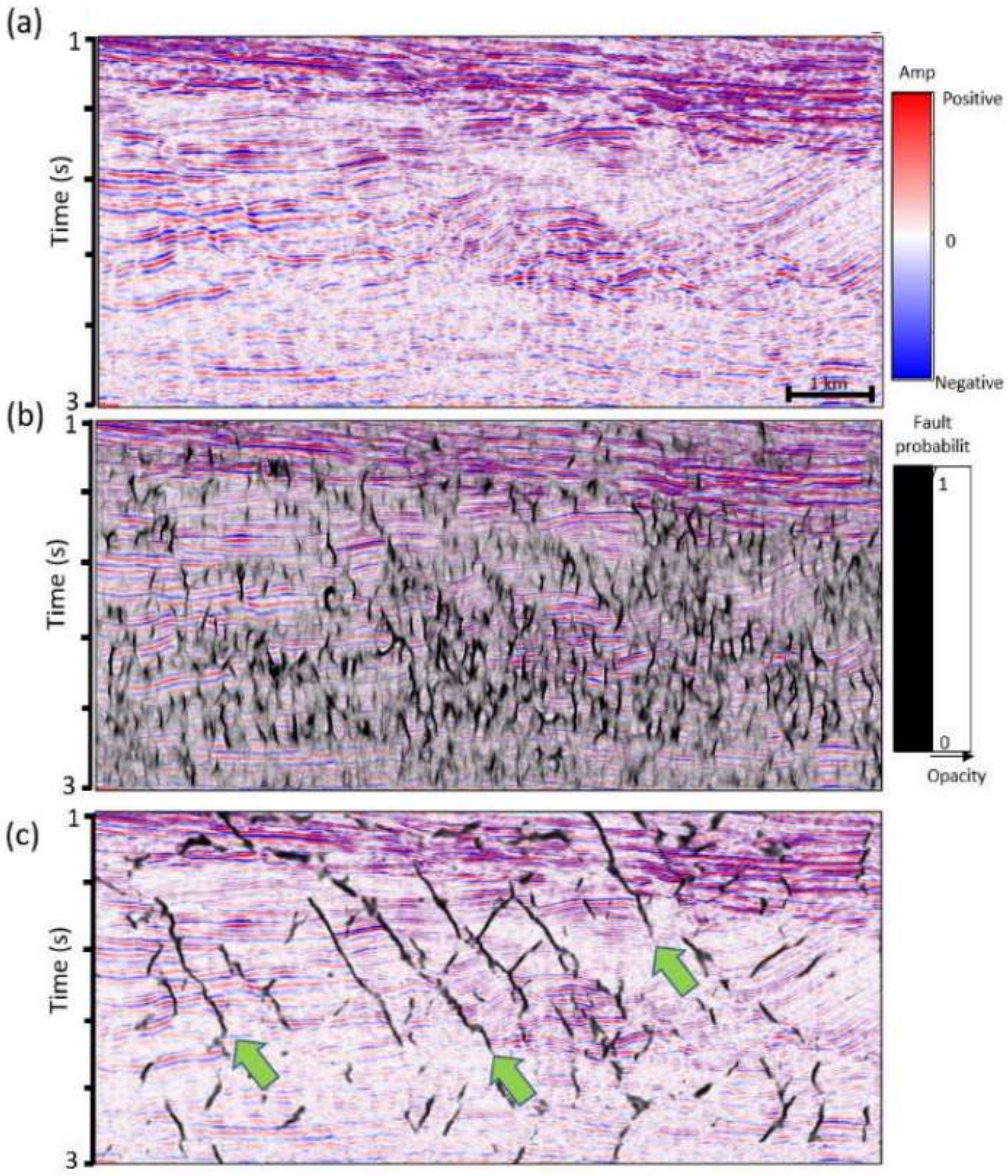

Figure 2 - Vertical slices through (a) seismic amplitude, (b) seismic amplitude co-rendered with fault probability computed using coherence as input, (c) seismic amplitude co-rendered with fault probability computed from the proposed CNN. Modified from Qi et a. (2017)

1.3.2. Fault Likelihood

Hale (2013) introduced an enhancement in the quality of fault attributes derived from 3D seismic data by utilizing fault-oriented semblance scans for fault detection. Hale's fault probability algorithm computes structure tensors at each image sample location within a 3D seismic volume, extracting local structural dips from these tensors. These dips are employed to smooth the seismic volume input along structural features and then to align adjacent traces in 3D after smoothing, allowing for the computation of a locally structure-oriented semblance.

Smoothing is essential here to condition the coherence calculation, which can become unstable if the semblance denominator approaches zero. It also reduces the sensitivity of the fault probability attribute to discontinuities introduced by spatially and temporally localized noise. The extent of this smoothing is governed by a parameter $\sigma_{\text{structure}}$, defining the half-width of the smoothing operator in sample space.

After computing the structure-oriented $semblance$, the algorithm performs a scan of the fault-oriented attribute. It searches for the fault strike and dip where the semblance value reaches a minimum, thereby maximizing the fault probability defined as $1 - s^8$, where s is the fault-oriented $semblance$ value. This scanning process requires smoothing the structure-oriented $semblance$ along all potential fault plane orientations so that coherent patterns offset by an actual fault are, in a sense, realigned through smoothing. The extent of smoothing along the fault planes is controlled by a parameter σ_{faults} which sets the half-width of the fault-oriented smoothing operator in sample space.

Wu and Hale (2016) expanded on this work by applying the fault probability attribute in conjunction with advanced fault tracking techniques. They found that this transfer significantly improved the ability to map fault systems, especially in areas with noisy seismic signals or complex geological structures.

In another case, Aqrawi and Boe (2011) applied the fault likelihood attribute to seismic data from the North Sea. They highlighted how this attribute could reveal intricate fault patterns in chalk reservoirs, which are often challenging to interpret due to their complex geology.

Wu et al. (2019) dive into seismic fault detection by comparing fault likelihood method with a pretrained Convolutional Neural Network (CNN) (Figure 3). This method leverages seismic attributes like coherence and semblance to estimate the probability of faults in the subsurface. It highlights discontinuities by analyzing changes in the seismic signal, providing a probabilistic map of where faults might occur. The comparison illustrates a shift towards embracing advanced machine learning techniques in geophysics.

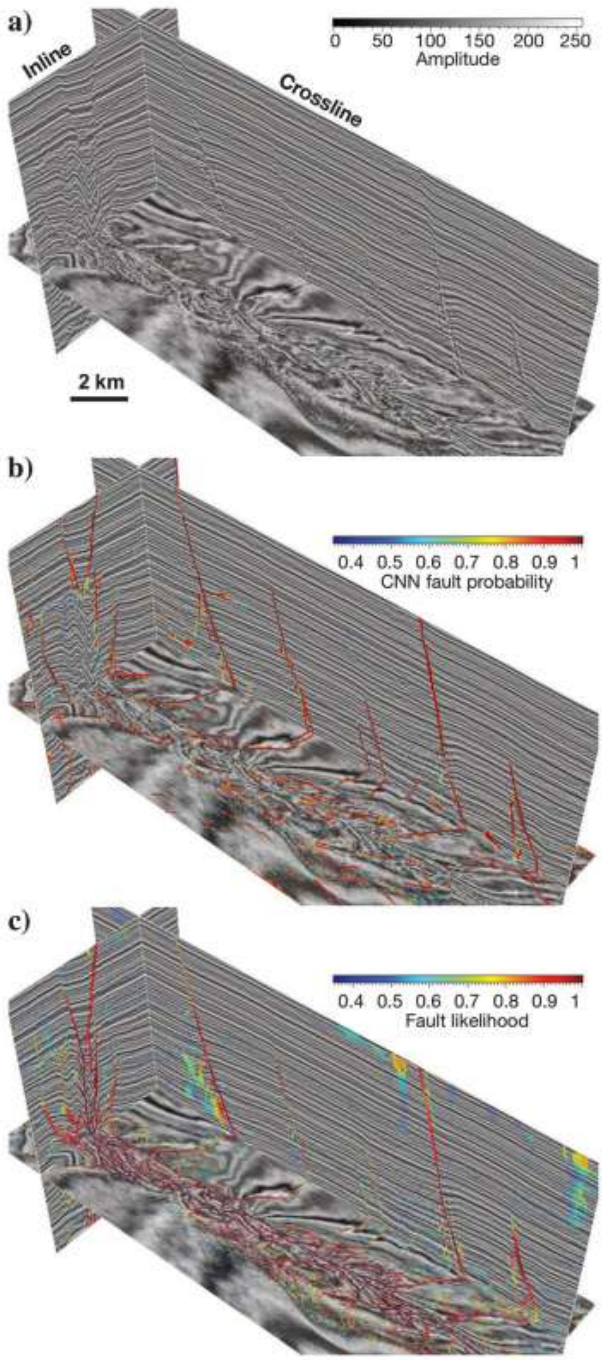

Figure 3 – A comparison between fault detection in (a) 3D seismic image using (b) the trained CNN model and (c) fault likelihood. Extracted from Wu et al. (2019).

1.3.3. Dip

The dip attribute provides insights into the inclination and orientation of subsurface geological features such as layers, faults, and folds. Precise dip estimation enhances the ability to construct detailed geological models, leading to improved hydrocarbon exploration and reservoir characterization.

Barnes (2016) defines dip in terms of inclination and azimuth. Let's first define inclination in 2D seismic data. In two-dimensional (2D) seismic data, the dip (p_x) in the x-direction is defined as the derivative of the depth (z) with respect to the horizontal distance (x):

$$p_x = \frac{\partial z}{\partial x} \tag{2}$$

This expression quantifies the rate of change of depth per unit of horizontal distance, effectively describing the slope of the seismic reflector in the x-direction.

In three-dimensional (3D) seismic data, the dip has components in both the x and y directions. The overall dip magnitude (p) is calculated using the gradient of the depth in both directions:

$$p = \sqrt{\left(\frac{\partial z}{\partial x}\right)^2 + \left(\frac{\partial z}{\partial y}\right)^2}$$

The dip angle (γ) is the arctangent of the dip magnitude, representing the angle between the seismic reflector and the horizontal plane:

$$\gamma \tan^{-1}(p), \tag{3}$$

where $p = \frac{|\partial z|}{|\partial x|}$ and ∂r is defined as $\frac{1}{\partial r^2} = \frac{1}{(\partial x^2 + \partial y^2)}$.

Gunther and Marfurt (2016) and Marfurt (2018) discuss various established methods for estimating dip-azimuth and dip magnitude in seismic volumes, all of which assume that seismic reflectors tend to locally align with a plane wave with constant dips (Figure 4). Therefore, for a 3D wavefield, u, with a constant dip, the wavefield can be approximated as:

$$u(x, y, z) \approx u(z - p_x x - p_y y) \tag{4}$$

Typically, slope scanning is performed within a small analysis window.

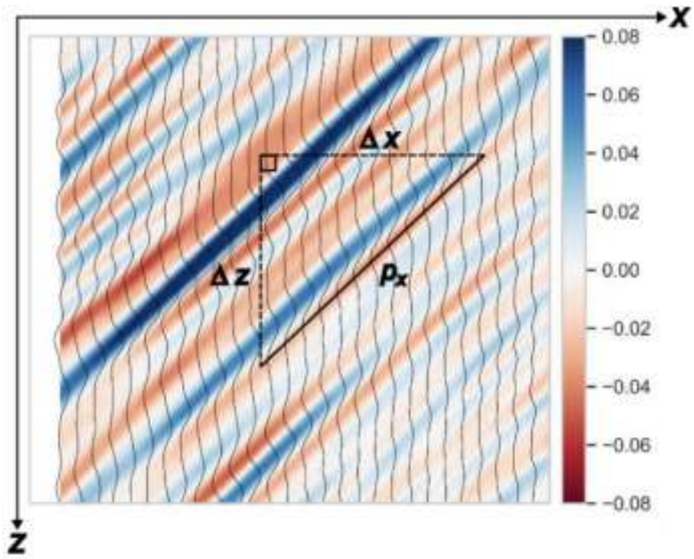

Figure 4 - Within a limited analysis window, seismic reflection data closely resembles a plane wave characterized by a constant dip. In this two-dimensional scenario, the dip is represented as $px \sim \Delta t \,/\, \Delta x$. Extracted from Oliveira Neto et al. (2023).

The method used for dip estimation in this work is called Gradient Structure Tensor Method, introduced by Bakker et al. (1999) and Randen et al. (2000), and it estimates dips by analyzing the directions of amplitude variation in seismic data. It identifies one direction with maximum variation — perpendicular to the reflection plane — and two with minimal variation that follow the reflections. They use Principal Component Analysis (PCA) to construct a 3x3 tensor from amplitude derivatives, which are calculated by convolving the seismic data with the derivative of a Gaussian filter. For example, to find the gradient in the x-direction, they convolve a Gaussian gradient operator g_x with the seismic data vector uu, obtaining the gradient vector G_x:

$$G_x = g_x * u(x, y, z) \tag{5}$$

An analysis of Gaussian filters underscores their effectiveness in mitigating noise while concurrently safeguarding the essential features present within a dataset. This dual functionality can be likened to the calibration of an optical lens, which sharpens the precision and clarity of key details while blurring out extraneous or distracting elements.

The same is done for the gradient vectors G_y e G_z. The complete gradient tensor, G, is defined by the three gradient vectors of each dimension:

$$G = \begin{pmatrix} G_x \\ G_y \\ G_z \end{pmatrix} \tag{6}$$

As highlighted by Randen et al. (2000), the estimation of the three-dimensional gradient vector serves as an effective representation of the local dip and azimuth inherent within the data (Figure 5).

The methodology in question is inherently vulnerable to contamination from noise and various artifacts, which necessitates careful interpretation. In an effort to mitigate the challenges presented by these distortions, one might consider the approach of smoothing the dip estimation. However, this raises concerns regarding the wrap-around effect, a phenomenon in which even a minor alteration in angle precipitates a significant shift in its representation — most notably observed through transitions, such as from -180 to +180 degrees. Such complexities render conventional smoothing techniques insufficient. In recognition of these intricacies, Randen et al. (2000) proposed a novel methodology that focuses on estimating the principal direction of the gradient vector as an alternative to the simplistic application of averaging filters. This technique effectively reduces the influence of noise and artifacts while maintaining the fidelity of dip and azimuth estimations.

In summary, while the gradient structure tensor method is powerful for dip estimation, careful consideration must be given to its inherent limitations and the potential need for advanced processing techniques to ensure accurate and reliable geological interpretations.

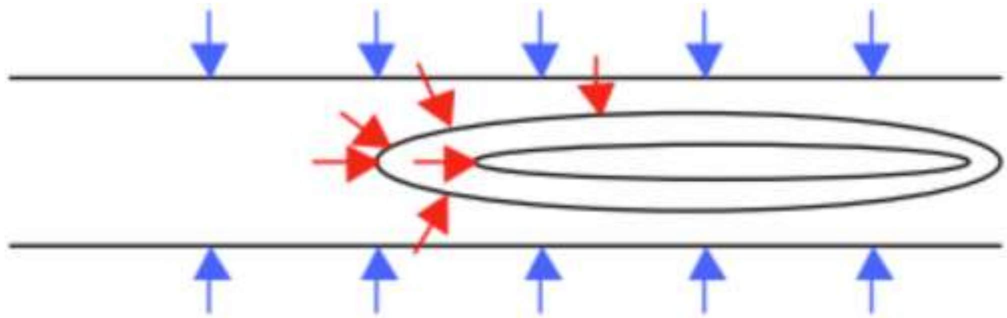

Figure 5 - Gradient estimates for a horizontal reflector with local amplitude variation. The black lines represent reflection amplitude contours, while the arrows indicate gradient vectors. From Randen (2000).

To estimate these directions, they first correlate the gradients, which means calculating the outer product of the complete gradient with itself, and then producing the gradient structure tensor:

$$G \cdot G^t = \begin{vmatrix} G_x^2 & G_x G_y & G_x G_z \\ G_y G_x & G_y^2 & G_y G_z \\ G_z G_x & G_z G_y & G_z^2 \end{vmatrix} \quad (7)$$

The elements of the tensor can be locally averaged to enhance gradient estimates while suppressing noise, though this process results in a loss of resolution. To optimize noise reduction versus resolution, Gaussian low-pass filters are applied within defined windows. Subsequently, Principal Component Analysis (PCA) is employed to extract the tensor's eigenvectors and eigenvalues. The dominant eigenvector e_1, corresponding to the maximal eigenvalue, indicates the direction of the greatest gradient, perpendicular to the reflection plane. By constraining e_1 to point downward, its components along the x, y, and z axes are denoted as e_x, e_y and e_z, respectively, facilitating the determination of dips p_x and p_y:

$$p_x = \frac{e_x}{e_z} \quad (8)$$

and

$$p_y = \frac{e_y}{e_z} \quad (9)$$

Figure 6 illustrates the definition following the above constraints.

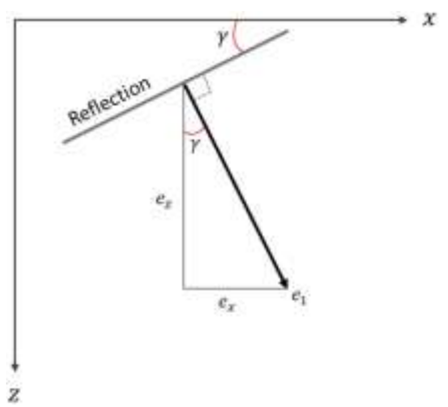

Figure 6 - The reflection dip p_x and the dip angle γ are found from the e_x and $e_y$of the eigenvector e_1, which is normal to the reflection. If the magnitude of the eigenvector e_1 is 1, then dip = $arccos\ e_z$. Modified from Barnes (2016).

In addition to robust seismic gradient, or dip, estimation, another advantage of this approach is the possibility of combining eigenvector information to produce other seismic attributes related to the reliability of the dip estimation and the "texture" of seismic amplitudes. However, such attributes are beyond the scope of this study.

Ao et al. 2021 discusses an innovative method to enhance seismic dip estimation using a deep learning approach (Figure 7). They highlight the integration of domain knowledge with deep learning techniques, addressing challenges like inaccuracies in traditional dip labels and the generalization gap between synthetic and field seismic data. By training a convolutional network on synthetic seismic samples followed by fine-tuning using field data in an iterative manner they demonstrate superior accuracy, robustness, and adaptability compared to traditional methods.

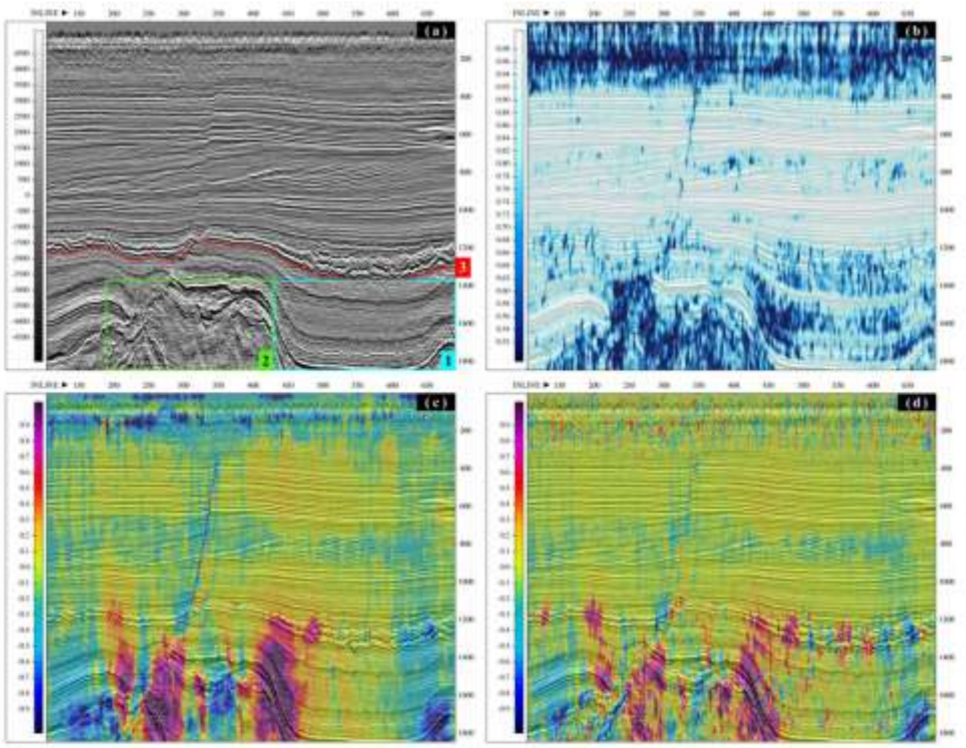

Figure 7 - F3 seismic data showing in (a) seismic amplitude xline and the corresponding coherence attribute in (b). Then, (c) is the network predicted xline dip profile and (d) scanned xline dip profile based on coherency profile illustrated in (b). Extracted from Ao et al. (2021).

1.3.4. Curvature

Curvature constitutes a family of geometric attributes extensively utilized in structural evaluation and geological interpretation (Chopra, 2009; Jesus et al., 2019; Correa et al., 2021). It is defined as the measure of deviation of a surface, at a given point, from a straight line or plane, effectively quantifying the rate at which the surface bends or changes direction. Mathematically, curvature is intrinsically related to the second derivative of a curve or surface, providing a quantitative assessment of its bending characteristics (Barnes, 2016). Higher curvature values indicate regions where the geological formations exhibit significant bending or folding, which is critical for identifying structural features such as faults, and fractures.

In 3D, as stated by Marfurt (2018), curvature involves calculating second derivatives of a real or implicit surface. For horizon-based curvature (e.g., Roberts, 2001), a local fit of a second-degree polynomial is performed given by:

$$z(x,y) = a\,\frac{\partial^2 z}{\partial x^2} + b\,\frac{\partial^2 z}{\partial x^2} + c\,\frac{\partial^2 z}{\partial x^2} + d\,\frac{\partial^2 z}{\partial x^2} + e\,\frac{\partial^2 z}{\partial x^2} + f \qquad (10)$$

Generally, nine or more grid points are used to calculate curvature on the chosen horizon (Figure 8). Using more points leads to a smoother curvature estimate, as demonstrated by Rich (2008). Curvature calculation involves determining eigenvalues (k1 and k2) and eigenvectors of a Hessian matrix given by:

$$k_{1,2} = \frac{cde - a(1+e^2) - b(1+d^2) \pm (\alpha - \beta)^{\frac{1}{2}}}{(1+d^2+e^2)^{\frac{3}{2}}} \qquad (11)$$

where:

$$\alpha = [a(1+e^2) - b(1+d^2)]^2\ , \qquad (12)$$

and:

$$\beta = [2bde - c(1+e^2)][2ade - c(1+d^2)] \qquad (13)$$

The corresponding eigenvectors (defining the azimuth perpendicular to a curvature lineament) are:

$$tan\theta_{\{1,2\}} = \frac{k_{\{1,2\}} - cde + 2b(1+d^2)}{2ade - c(1+d^2)} \qquad (14)$$

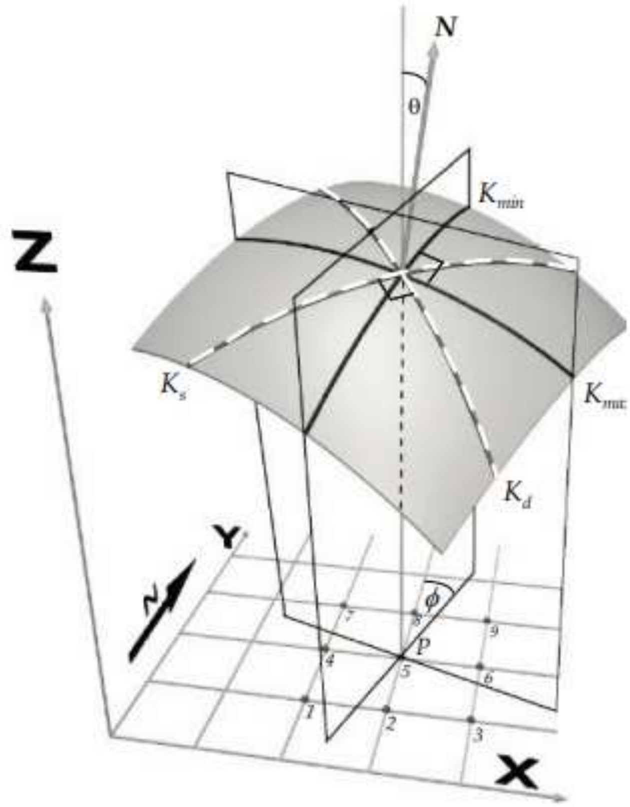

Figure 8 - Three-Dimensional Curvature Analysis. The axes denoted as X and Y correspond to spatial dimensions, while Z represents the temporal or depth dimension. The intersection of two perpendicular planes with the surface is highlighted, delineating the maximum curvature, K_{max}, and the minimum curvature, K_{min}. Additionally, the surface presents two other orthogonal normal curvatures: the dip curvature, K_d, and the strike curvature, K_s. The vector N signifies the surface normal at point P, forming an angle θ with the vertical axis, known as the dip angle. The orientation of any normal curvature can also be extracted, with the angle ϕ being the orientation of the minimum curvature. Extracted from Roberts (2001).

The direction in which we measure the surface deformation defines the curvature measurement. The principal directions of curvature are the most positive and most negative curvatures, k_1 and k_2, respectively. From this pair, other curvature attributes can be derived, such as maximum and minimum curvature; however, they will not be discussed in this study. In practice, curvature attributes analyze how much a surface is deformed at a given point and are generally applied to locate dips and structural highs and lows.

Oliveira Neto et al. (2023) investigates the use of geometric seismic attributes, specifically curvature, to characterize fractured zones in pre-salt lacustrine carbonates. By evaluating different curvature estimation methods and correlating them with borehole-derived fracture intensity logs, they identify the most effective curvature parameterizations for delineating fracture-prone intervals (Figure 9).

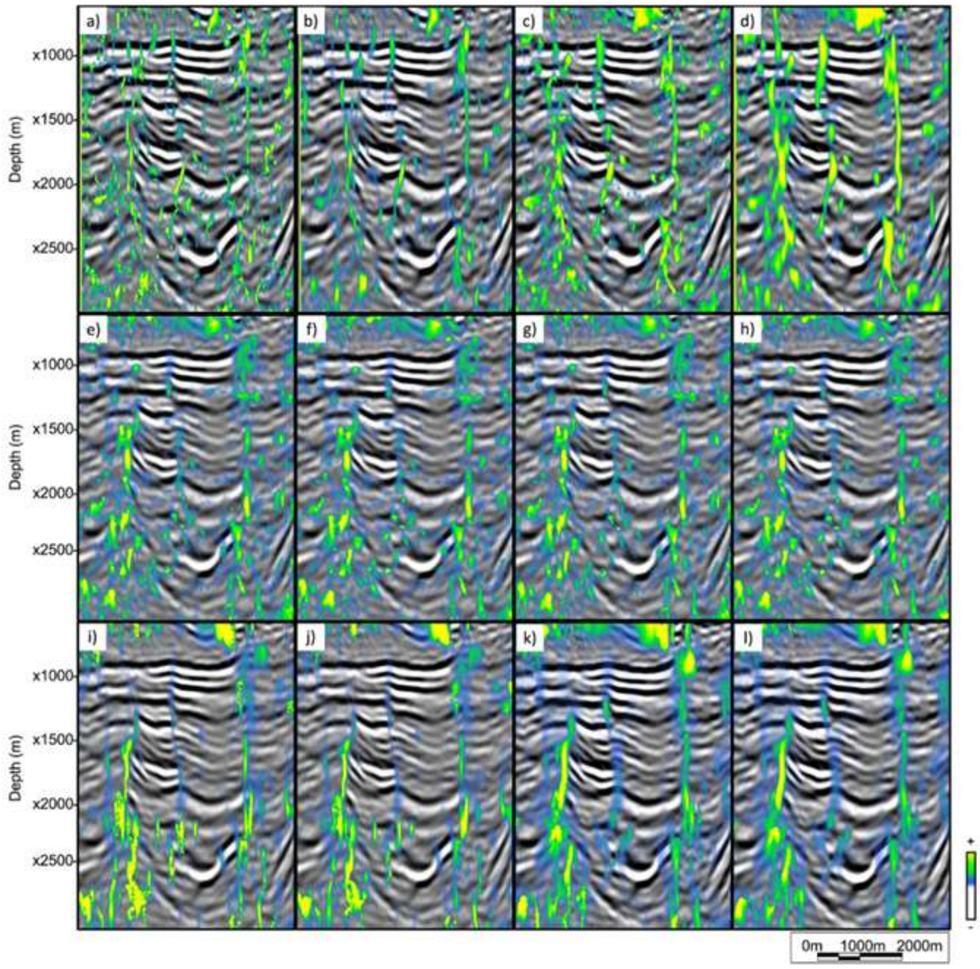

Figure 9 - Seismic panel of the seismic amplitude data from Mero field showing the evaluation of different filtered curvatures. Extracted from Oliveira Neto et al. (2023).

1.4. A review of artificial intelligence

The first problem one might encounter when referring to artificial intelligence (AI) is its definition. According to Russell and Norvig (2021), the definition of AI depends on objectives of the practitioner. It changes whether the objective is to mimic human behavior or simply make the optimal decision in a specific situation. And it may also change depending if the focus is on the process of thinking or just the resulting behavior of the system in question.

For our purposes, the more pragmatical definition adopted by Russell and Norvig (2021) is used: an intelligent agent takes the best possible action in a scenario and the field of Artificial Intelligence studies how to create such agents. In this view, tools commonly used that are not seen as intelligent, such as automatic tracking of seismic horizons, can be considered as AI techniques.

It then becomes necessary to define a subfield of AI in which the intelligent system can learn its decision-making rules by itself based on data. The algorithms and methods that fall under this category are what is called Machine Learning (ML). Machine learning methods comprise a plenty of methodologies for data analysis aiming to automate the building of advanced analytical data-driven models (Figure 10) (Holdaway and Irving, 2017). As an example, Artificial Neural Networks (ANN) is a machine learning tool for solving difficult problems due to their ability to identify complex relationships between the various variables (Aminian et al., 2005; Esmaeilzadeh et al., 2013).

Neural networks often have applications when relationships are too complicated or require a long-term process to solve with conventional methods. For the oil industry, neural networks are quite useful, as they are a great tool for identifying the relations among porosity, permeability, acoustic impedance, flow units, fluid saturations, depositional environments, lithology and well log data (Aminian et al., 2005; Jesus et al., 2019; Ferreira et al., 2021b).

The main differential of neural network methods compared to traditional statistical methods are: (i) the ability to extract nonlinear relationships between the input data and target values; (ii) no model of linearity or other assumptions are needed; (iii) good behavior with ambiguous and noisy data and (iv) there is no need to know the underlying statistical distribution of the input data (Trappe et al., 2000, Leite et al., 2011).

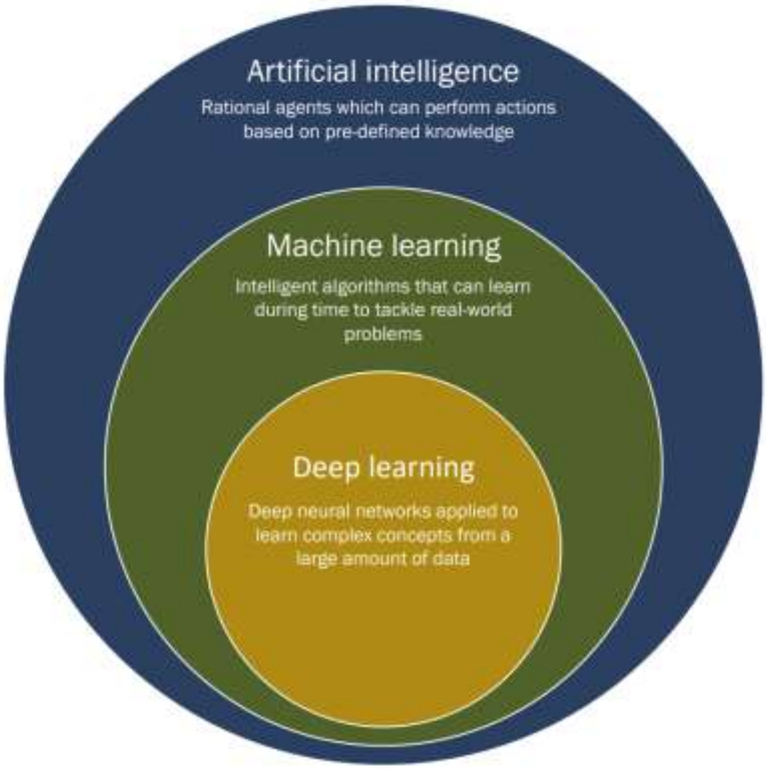

Figure 10 - Illustration of the relationship between the fields of Artificial Intelligence, Machine Learning and Deep Learning.

Following Mitchell's (1997) definition "a computer program is said to learn from experience E with respect to some class of tasks T and performance measure P, if its performance at tasks in T, as measured by P, improves with experience E." The different algorithms in this class will differ not only based on the task T, the measure performance measure P and what defines the experience E, but also based on how this process is executed, i.e., how the algorithms learn.

For the specific goals of this chapter, the task in question is the segmentation of seismic data according to its seismic facies. In practical terms, the system will receive as input seismic attributes and outputs the seismic facies, porosity or flow facies distribution on the same volume. The performance measure here is simply a level of accuracy of the system predictions. If the facies, porosity or flow facies obtained match closely those given by a human interpreter or information from well logs, the performance score would be high and in the opposite case it would be lower. More precise definition on this performance score will be given later.

Finally, the experience from which the algorithm learns from will subdivide the ML field in two major subgroups: unsupervised learning and supervised learning (Goodfellow et al., 2016). In an unsupervised learning method, the learning comes from the structure of the data itself, without the presence of a prior correct answer on which it can compare its predictions.

The algorithms used here fall under the latter category, supervised learning. In this type of methods, it is necessary present the system with both the input data and the expected answer, often called label. These pairs of input data and corresponding labels is called training dataset. Again, for this chapter purposes, the input data is seismic attributes cubes and labels are the interpretation of a human interpreter and/or well logs.

It is important to note that this distinction between unsupervised and supervised learning is not too strict. According to Goodfellow et al. (2016), many machine learning techniques can be used in both ways, presenting more aspects of one or the other depending on how the learning occurs. Also, they point out that are other possible classes of methods based on how they learn from data, such as reinforcement learning.

There are several supervised learning methods, with varied strategies for performing specific tasks, such as Linear Discriminant Analysis, Logistic Regression, Decision Trees, Support Vector Machines, Nearest Neighbors, among many others (Hastie et al.; 2009). The class of algorithms chosen for the problem of seismic facies classification is the Convolution Neural Networks and for 3D modelling of porosity and flow facies are Fully Connected Neural Networks and Decision Trees (Random Forest method) in the Mero Field.

1.4.1. Neural Networks

Neural networks, also called artificial neural networks and sometimes multilayer perceptron, are a large class of machine learning models that can be applied in a range of different fields. Neural networks (NN) received their names because its behavior is loosely based on the human brain. The first recordings of neural networks came from McCulloch and Pitts (1943), who devised a simple mathematical model for the functioning of a neuron. The other part of the name comes from the fact that the artificial neural network basic units (also called neurons) are connected to each other in a network fashion, with neurons on one layer receiving inputs from the neurons of the previous layer and sending their outputs to the neurons on the following layer (Figure 11).

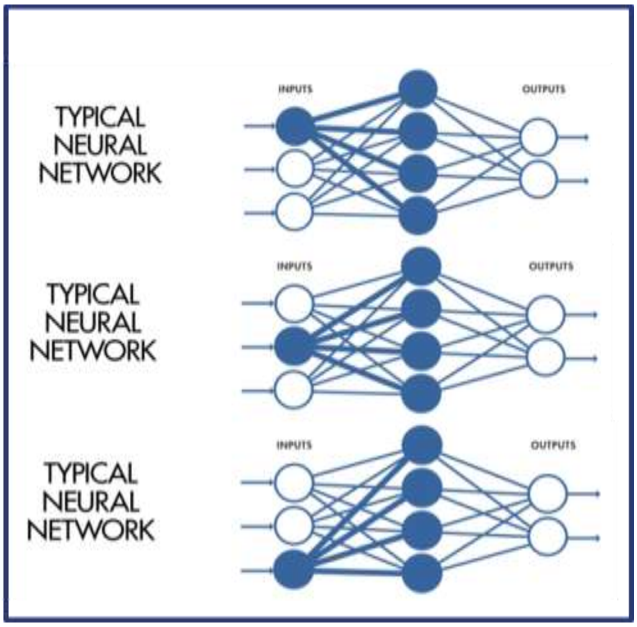

Figure 11 - Operation of an artificial neural network. Nodes are represented as blue spheres and the weights blue lines. Source: https://www.mathworks.com/videos/introduction-to-deep-learning-what-are-convolutional-neural-networks--1489512765771.html

Following Russell e Norvig (2021), the mathematical functioning of a neuron in a neural network is given:

$$a_{l,j} = g(w_{l,0,j} + \sum_1^n w_{l,i,j} a_{l-1,i}), \qquad (15)$$

where $a_{l,j}$ is the activation of the neuron j on the layer l, g is the activation function and $w_{l,i,j}$ are the weights of the neuron j on the layer l, with the specific weight $w_{l,0,j}$ being called bias. The activation function g is a non-linear function of its inputs and can be a hard threshold, in which case the neuron is called a perceptron, or a sigmoid-like function (soft threshold), as seen in Figure 12. The Eq. 15 can also be written in a vectorial form:

$$a_l = g(\boldsymbol{b}_l + \boldsymbol{W}_l \cdot \boldsymbol{a}_{l-1}), \qquad (16)$$

with bold letters representing vectors and bold capital letter representing matrices.

Even with this simple structure it can be shown that a single layer neural network can be used to approximate any piecewise differentiable function with arbitrary precision (Hornik et al.; 1990).

There are other types of network architectures besides the ones showed here. These simple types of networks are sometimes called vanilla neural networks. Some other architectures include recurrent neural networks (RNNs), in which the data does not move only forward, with possible loops; and convolutional neural networks (CNNs), which basically replace the neuron with convolutions. This last type of networks is the one that will be used here for seismic fault segmentation and will be covered in more detail.

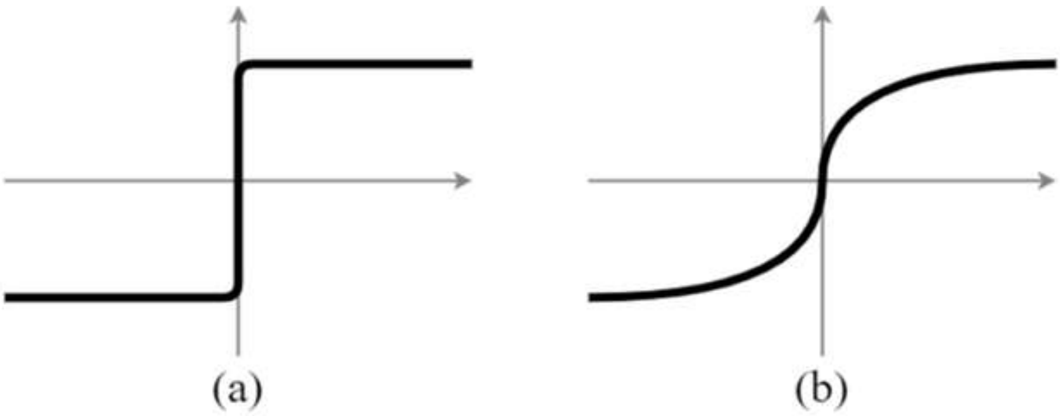

Figure 12 - Perceptron activation function (a) and sigmoid-like activation function (b).

When the neurons from a layer in a neural network are connected to all the neurons on the next layer, this network is commonly called Fully Connected Neural Network (FCNN, Figure 11). That was for a long time the most popular neural network architecture and it is useful to predict specific properties from the training process of input data. It is a supervised regression and quantification method, this means that they are trained with both input and target vectors (Esmaeilzadeh et al., 2013). Linear combination functions estimate a linear combination between the weights and the current values into the neurons and then adds the bias value. And the sigmoid functions are S-shaped functions (such as the logistic and hyperbolic tangent functions, Figure 12b) that produce values within a range of 0 to 1 or −1 to 1 (Holdaway and Irving, 2017).

In the application of neural networks, the training, test and validation processes are the three fundamental steps (Esmaeilzadeh et al., 2013). This requires that the available data be divided into three groups. The training set effectively trains the neural network and must be representative for the general solution sought by the neural network (Holdaway and Irving, 2017). A data set performs tests during the training of the neural network, alongside the process of weights and bias values adjustment. The validation (or application) dataset is used as a blind test that validates the neural network.

One of the key parameters behind the building of the FCNNs architecture is the number of hidden layers and neurons in each layer. When a neural network is applied to seismic data to identify reservoir properties, it is important to select the parameters of the neural network well to avoid problems such as data overfitting or underfitting. A bad choice of parameters – such as number of hidden layers, percentage of data for testing, number of iterations, among others – can result in a poor estimation that does not represent well the data set and the geological characteristics of the region.

1.4.2. Training process

When constructing a neural network, besides the choice regarding its topology (number of layers, number of neurons in each layer), another question is what the weight values should be ($w_{l,i,j}$ in Eq. 15). It is virtually impossible to come up with the optimal values of the weights by just knowing the problem being solved. For this reason, first it is necessary to compute weight values that are optimal or close to optimal for the task in question. This step of computing weights is called training of a neural network.

The most common algorithm for training the network is to use the iterative process known as gradient descent method:

$$W_{i+1} = W_i - \alpha \nabla_W C(O_k; G(I_k, W_i)), \tag{17}$$

where W_i represents all weights of the network at iteration i, α is the learning rate, ∇_W is the gradient with respect to the weights, C is the cost function (a function that computes the error of the network), O_k is the desired input of the network for input I_k and G is a function that represents the propagation of the network following Eq. 15. Note that by definition:

$$G(I, W) = a_L, \tag{18}$$

where a_L is the output vector of the last layer of the network and L is the number of layers.

As shown in Eq. 16, this process requires the calculation of the gradient of the error of the network with respect to all its weights. The most used process for doing this computation is known as backpropagation (Rumelhart el al., 1986). As suggested by its name, this process consists of calculating first the gradient with respect to the weights of the last layers and then using this result to compute the gradients for each previous layer in a sequential way.

The backpropagation algorithm starts by defining the error for the output layer as:

$$\boldsymbol{\delta}_L = \nabla_{a_L} C \odot g'(\boldsymbol{b}_L + \boldsymbol{W}_L \cdot \boldsymbol{a}_{L-1}), \tag{19}$$

where $\boldsymbol{\delta}_L$ is the error for the last layer L, $\odot$ represents element-wise product between two vectors or matrices and g' is the derivative of the activation function. Note that the error for the last layer depends only on the error of the network, computed by C. For each previous layer, the error depends on the error of the following layer, defined by the following equation:

$$\boldsymbol{\delta}_l = (\boldsymbol{W}_{l+1}^T \boldsymbol{\delta}_{l+1}) \odot g'(\boldsymbol{b}_L + \boldsymbol{W}_L \cdot \boldsymbol{a}_{L-1}), \tag{20}$$

in this case the error depends only on the weights and errors of the next layer. For this reason, the process of backpropagation is performed from the last to the first layer. The gradient of the network can be computed with respect to each of the network layers using the previous definitions:

$$\frac{\partial C}{\partial w_{l,i,j}} = a_{l-1,i}\delta_{l,j}, \tag{21}$$

and:

$$\frac{\partial C}{\partial b_{l,j}} = \delta_{l,j}, \tag{22}$$

The backpropagation process defines a way to obtain the gradient $\nabla_W C$ present in Eq. 17. It depends on an input I_k and its respective desired output O_k. For this reason, this process is repeated in an example-by-example basis. In other words, the process is repeated for a set of example pairs (I, O) with the weights of the network being updated at each iteration. This set of examples used for obtaining the optimal values for the weights is called the training dataset.

1.4.3. Convolutional Neural Networks

Convolutional neural networks (CNNs) are a type of neural networks well suited for application in data that has a defined grid structure (Goodfellow et al.; 2016), such as images and, more interestingly, seismic volumes. As the name states, the main difference between these networks and the vanilla neural networks is that CNNs utilize a mathematical operation called convolution.

Mathematically speaking, a convolution is an operation done between two functions that blends then together producing a final function that is defined:

$$h(t) = f * g = \int_{-\infty}^{+\infty} f(x) \cdot g(t-x)dx \ , \qquad (23)$$

where f and g are the functions, t is the domain variable, x is the integration variable and h is the convolution. The $*$ operator is used to denote the convolution operation. The same process can be generalized for the discrete case and for multiple dimensions.

Another way to interpret convolutions consists in fixing one of the functions and sliding the other function over it. For each position that the sliding function moves, the resulting value of the convolution is the area of the product of the functions. This interpretation is convenient to understand discrete convolutions in two dimensions, as shown in Figure 13.

The multidimensional discrete convolution is the building block for convolutional neural networks. In CNNs the traditional matrix multiplications (Eq. 16) are replaced by these convolutional operations and for this reason can deal with 2D (or higher dimensions) data keeping its structure. According to Goodfellow et al. (2016), there are three main ideas behind this change: sparse weights, parameter sharing and equivariant representations.

Sparse weights means that convolutional neural networks use much less parameters than a fully connected neural network to perform its basic operations. It is accomplished by the fact that the kernels of a CNN are usually much smaller than its input (for example, in Figure 13, the input has size 4x3, while the kernel has size 2x2, meaning that only 4 parameters are needed to perform the convolution, i.e., the elements of the kernel). Meanwhile, in the case of the vanilla neural network shown in Figure 13, going from the layer k−1 to k needs at least 6 parameters (one for each connection, disregarding the biases). The difference is that the 2x2 kernel convolution can be applied to any size of 2D arrays, while increasing the number of neurons in a layer of a fully connected network will increase the number of weights proportionally. The calculation of this type of convolution is also much more efficient than the matrix multiplication, requiring fewer operations.

Parameter sharing is the other concept that arises because of the nature of discrete convolutions that benefits CNNs. This concept is tied to the sparse weights concept discussed before. It is easing to understand it by going back to Figure 13, where the parameter y, for instance, is used in the computation of all output values. Meanwhile, following Eq. 15 for the traditional neural networks, when moving from one layer to the other, each parameter (weights) is used exactly once. The reuse of parameters can help improving training and reduce the memory consumption of CNNs.

Lastly, equivariant representation denotes that if a change happens on the input of a convolution, the same change will be observed on the output. Specifically, convolutions have the property of being equivariant to translation, meaning that shifting its input by any amount will cause an equivalent shift on its output. The same is not true for fully connected neural networks.

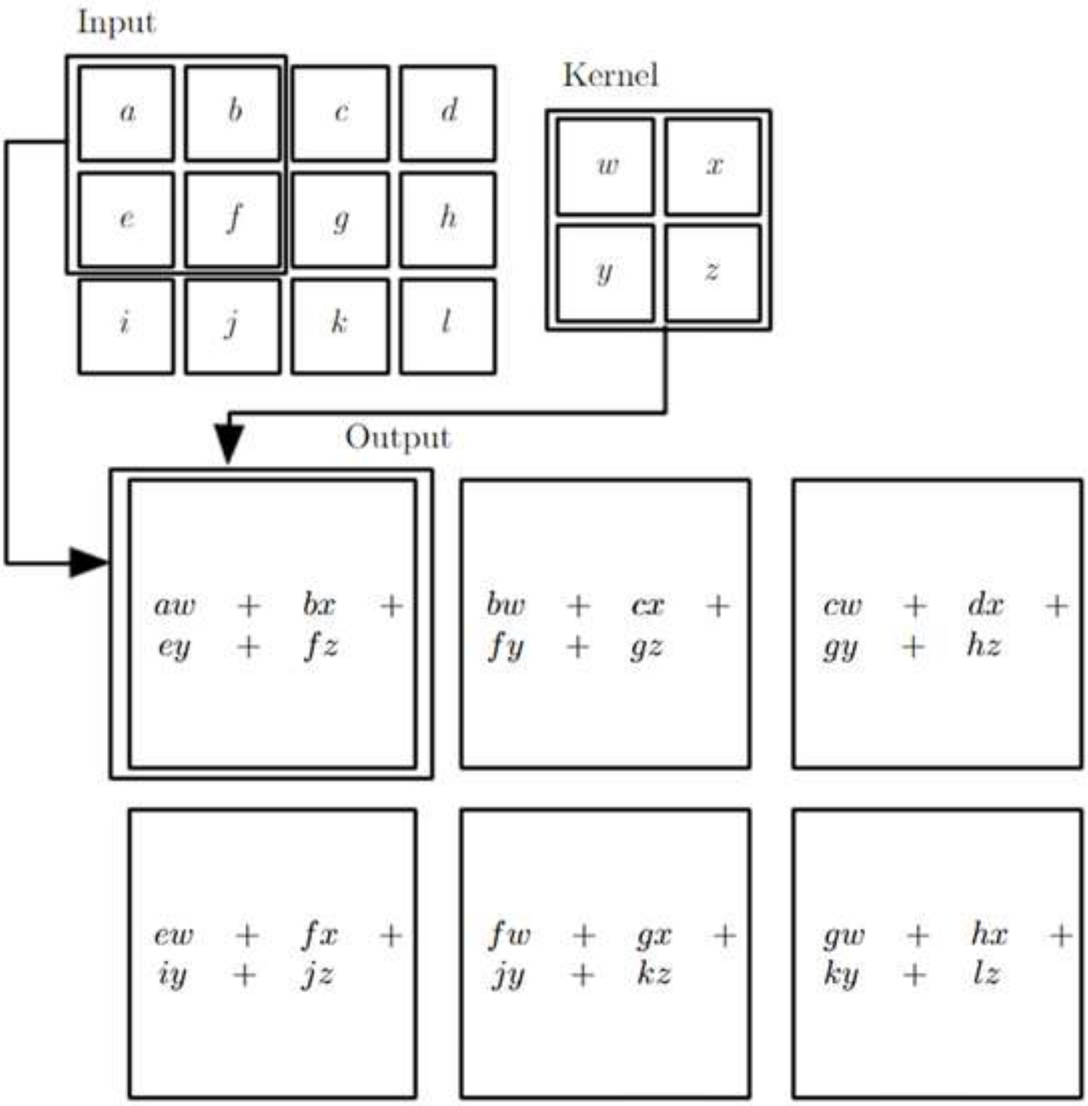

Figure 13 - Example of convolution, where the Input array remains stationary, and the kernel slides over it. Each position of the Output is defined as the sum of the element-wise product of the two arrays. The superposition to calculate the first Output element is indicated by the boxes and arrows. Observe that in practical implementations for Convolutional Neural Networks, none of the arrays are flipped, as shown on the definitions (Goodfellow et al., 2016).

Figure 14 synthetizes all the three fundamental aspects of the discrete convolution. The fact that the kernel has only 2 parameters illustrates the concept of sparse weights, in the sense that only these 2 parameters are needed to compute this specific operation no matter the size of the input. Also, the same two parameters are reused throughout the image when the kernel slides over it, which exemplifies the parameter sharing idea.

Lastly, when a vertical shift is applied to the input, the result is a vertical shift on the output, showing the equivariance to translation.

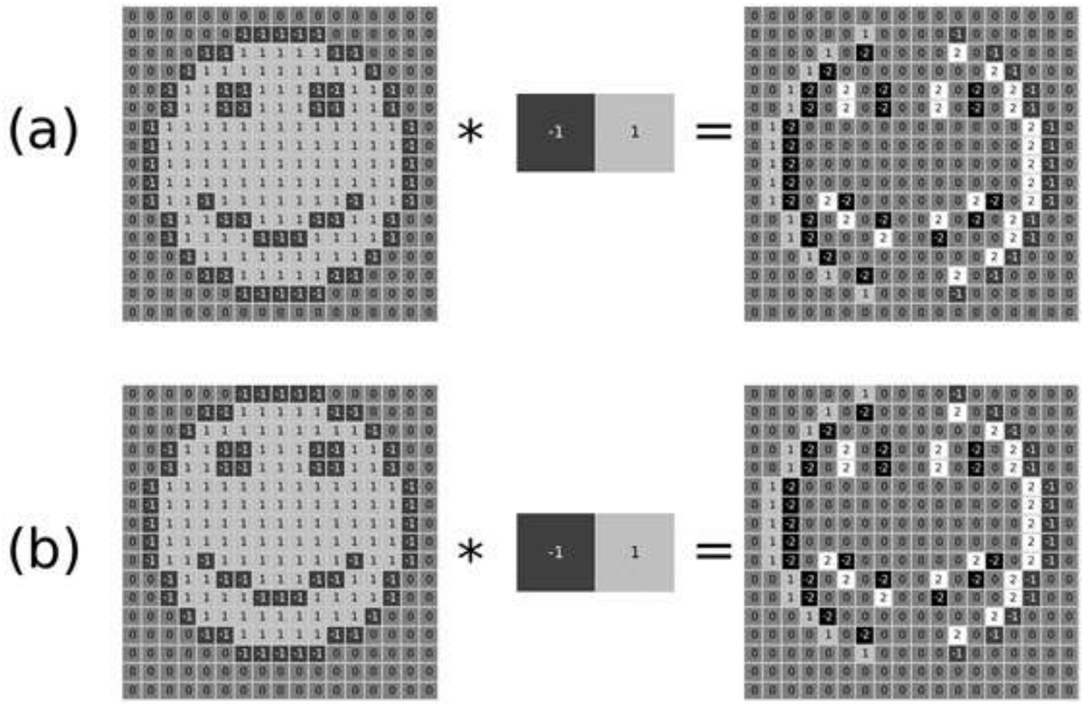

Figure 14 - Convolution of a 17x17 image and a 2x1 kernel. This specific operation is the derivative in the horizontal direction and can be used as an edge detection feature. Observe that when shifting the image from (a) to (b), the output of the convolution is the same as before, but with the same shift applied to it, showing the equivariance to translation property.

It is important to note the difference in representation between CNNs and vanilla neural networks. The CNN equivalent of a neuron in a vanilla neural network is a convolution kernel. And as a neural network neuron can have many neurons, a layer in a CNN can have many convolution kernels. This is usually represented as a cuboid shape, with one dimension denoting the number of kernels and the other two dimensions representing the shape of its inputs, as illustrated in Figure 15. More details on the actual implementation of CNNs and the mathematical formulation of the training process of neural networks will be covered in the next section.

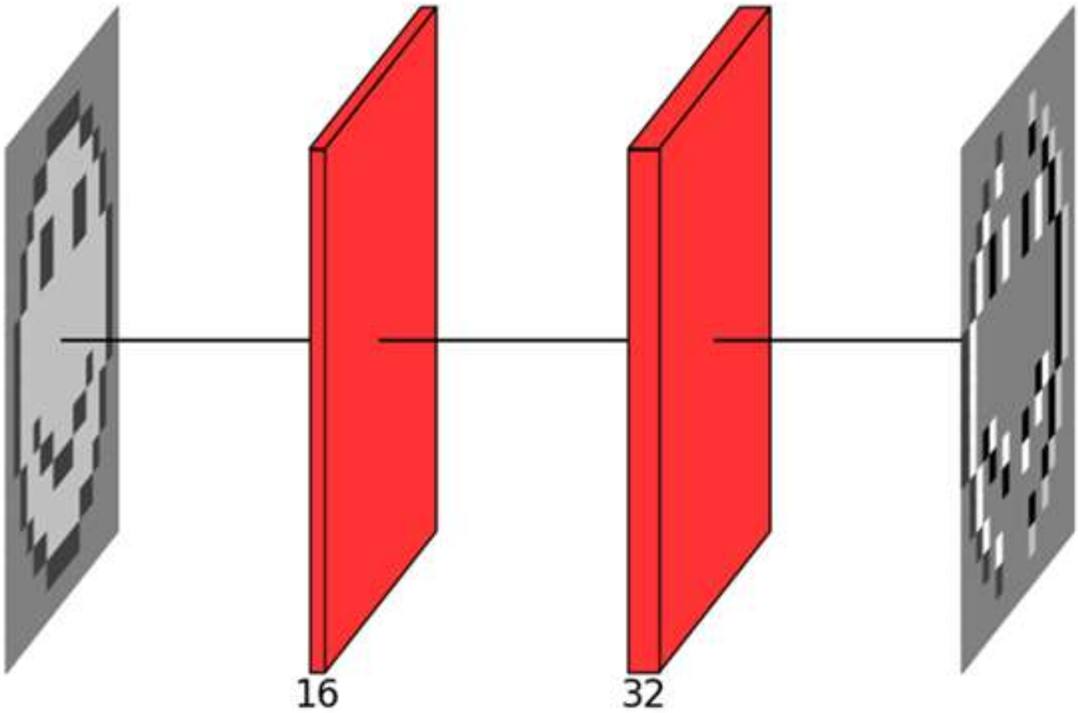

Figure 15 - Representation of a simple convolutional neural network with two convolutional layers. The layers are represented by the red cuboids. The numbers below the layers indicate the number of kernels, i.e., the first layer has 16 kernels and the second layer, 32.

1.4.3.1. Convolution layers

The convolutional layer is the main building block of a convolutional neural network. It computes discrete multidimensional convolutions on its inputs, outputting images with the same number of dimensions. A convolutional layer usually is considered to have 4 parameters: the number of convolution kernels, the shape of the kernels, the stride and whether it uses padding.

The number of kernels defines the number of independent convolution operations that will be performed, as well as the number of output elements. The shape of the kernel defines the dimension of each of those convolutional filters and is usually much smaller than the size of the layer input. For convolutional layers, their weights are tensors (multidimensional arrays) with the first-dimension accounting for the number of channels on the input and the last dimension for the number of kernels. The other dimensions define the size of the kernel. For instance, if the input has 5 channels and the layers have 16 kernels of shape 3x3, the weights for this layer are a tensor with dimensions 5x3x3x16.

The stride defines how many steps the kernel will move in each step of computing the convolution. And the padding is used to be able to cover the borders of the input, in which case a few extra elements with value 0 are added to it. All these elements are illustrated in Figure 16. In this example, the input is an image of size 7x7 and 3 channels. The convolutions have 2 kernels with shape 3x3 and stride 2. Also, in this case padding was used. With this configuration the weights have shape 3x3x3x2 and the output is shaped 3x3 and 2 channels.

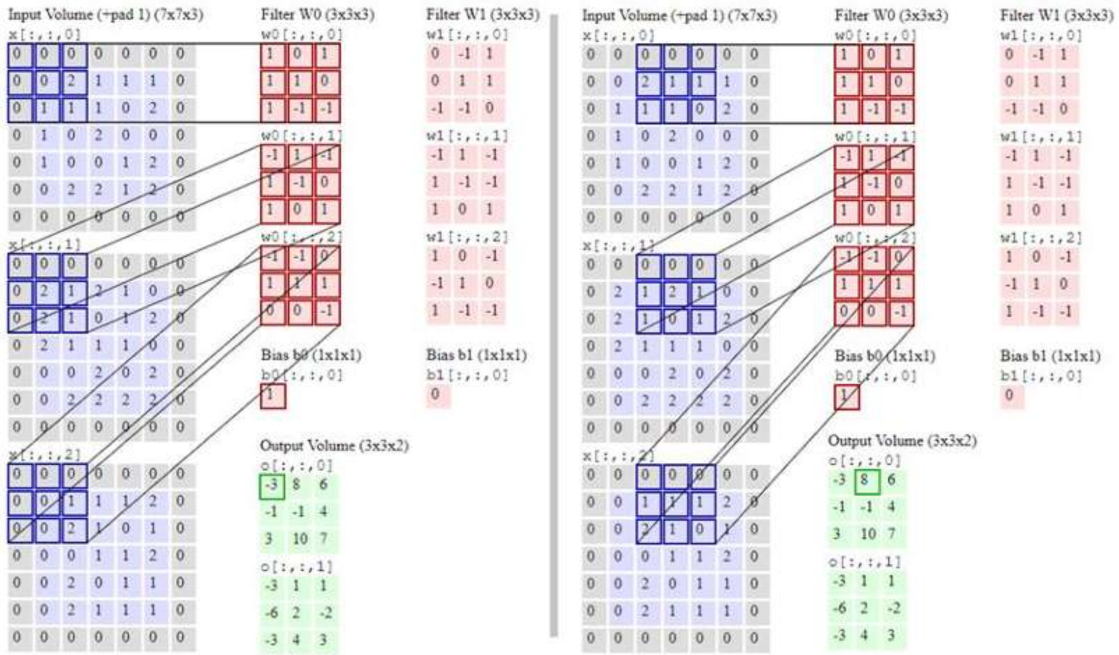

Figure 16 - Two steps of a convolution step in a convolutional layer. Blue squares are the input. Red squares are the convolution kernels. Green squares are the output. Gray squares are the zero padding. The input has a shape of 3x7x7, the weights have shape 3x3x3x2 and the output has shape 2x3x3. Note that from the first step (left) to the second step (right) the kernel moved by two positions due to the stride value of 2. Modified from: cs231n.github.io/convolutional-networks.

1.4.3.2. Activation functions

The activation functions are applied after a convolutional layer to introduce nonlinearity to the neural network model and allow it to learn non-linear mappings. For a long time, the most used activation function was the sigmoid (Figure 12b). However, according to (Goodfellow et al., 2016), the current default for activation function is the Rectified Linear Unit (ReLU; Nair and Hinton, 2010). The ReLU has some good properties for learning convergence, like being piecewise linear. It is defined as the following:

$$g(a) = \begin{cases} 0, if\ a\ \leq 0 \\ a, if\ a\ > 0 \end{cases}, \qquad (24)$$

The other activation function used in the CNN developed here is the Softmax function. The main desired characteristic of the Softmax function is that it takes its inputs and outputs them in a way that each one of them has values between 0 and 1 and their sum is 1. This makes it possible to interpret the outputs of a Softmax activation function as a probability distribution. The equation that is used to compute the Softmax activation is the following:

$$g(\boldsymbol{a}) = \frac{e^{a}}{\sum_i e^{a_i}}, \qquad (25)$$

1.4.3.3. Batch normalization

The batch normalization step (Ioffe and Szegeby, 2015) is a regularization technique for convolutional neural networks that helps to speed up the training process. It does so by guaranteeing that during training the output of the layers where batch normalization is performed will have the same mean and standard deviation. This normalization happens along with all examples in a batch.

1.4.3.4. Downsampling and upsampling

When data is propagated through a network, it is common practice to reduce its size to reduce memory consumption and improve network performance. This process is called downsampling or pooling. One of the main strategies for downsampling is called Max Pooling. In this strategy, the output of a layer is tiled into small regions and for each of those regions only the maximum value is passed ahead for the next layer. This process is illustrated on Figure 17. Besides improving performance and reducing memory consumption, the Max Pooling process has the benefit of increasing the tolerance of the network for small movements on its input. This happens because even if the output of a layer is dislocated by a few samples, the Max Pooling operation might still yield the same output.

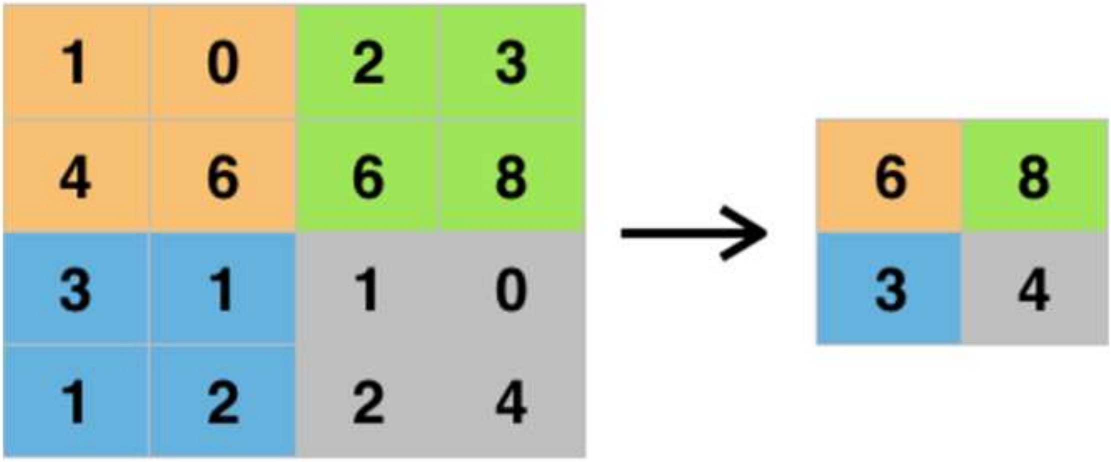

Figure 17 - Example of a Max Pool operation performed on a 4x4 array. The input array is divided in 4 regions and for each of these regions only the maximum value is used in the output. This operation reduces the size of the array from 4x4 to 2x2. Available online at deepai.org/machine-learning-glossary-and-terms/max-pooling.

The reverse process of downsampling is upsampling and it is used when the output of the network needs to have the same dimensions of its input after going through some downsampling operations. One of the ways this effect is achieved is by repeating the values of the output of a layer in a grid-like arrangement, like the splitting regions in the Max Pooling.

1.4.3.5. Automatic seismic fault detection

The integration of deep learning techniques into seismic fault detection has significantly transformed the landscape of seismic data interpretation, providing unparalleled accuracy and efficiency. Traditional methodologies frequently encountered challenges associated with the complexities and noise characteristic of seismic datasets. In contrast, deep learning models, especially Convolutional Neural Networks (CNNs), have exhibited exceptional capabilities in the identification and delineation of fault structures within seismic volumes. This advancement not only enhances the precision of fault detection but also streamlines the interpretation process, marking a notable progression in the field of seismic interpretation.

Wu et al. (2019a) established a seminal benchmark in the realm of seismic fault detection using deep learning. By introducing an open-source comprehensive framework, they democratized access to advanced convolutional neural networks (CNNs) tailored for identifying faults in seismic data. Their work not only showcased the effectiveness of CNNs in capturing complex geological features but also set a precedent for transparency and collaboration in the field.

Zhao and Mukhopadhyay et al. (2018) and Di et al. (2018) contributed significantly by presenting innovative deep learning strategies for seismic fault identification. They focused on optimizing network architectures to better handle the unique challenges posed by seismic data, such as noise and varying signal characteristics. Also, they explored the depths of deep learning applications in geophysics by introducing models adept at handling the complexities of seismic data. They addressed challenges such as varying fault orientations and noise interference, proposing solutions that enhanced the robustness of fault detection algorithms.

At last, An et al. (2021) introduced CNN architectures with novel loss functions specifically designed for edge detection in seismic images (Figure 18). Recognizing that faults often manifest as edges, they developed models that excelled at highlighting these critical features while suppressing noise.

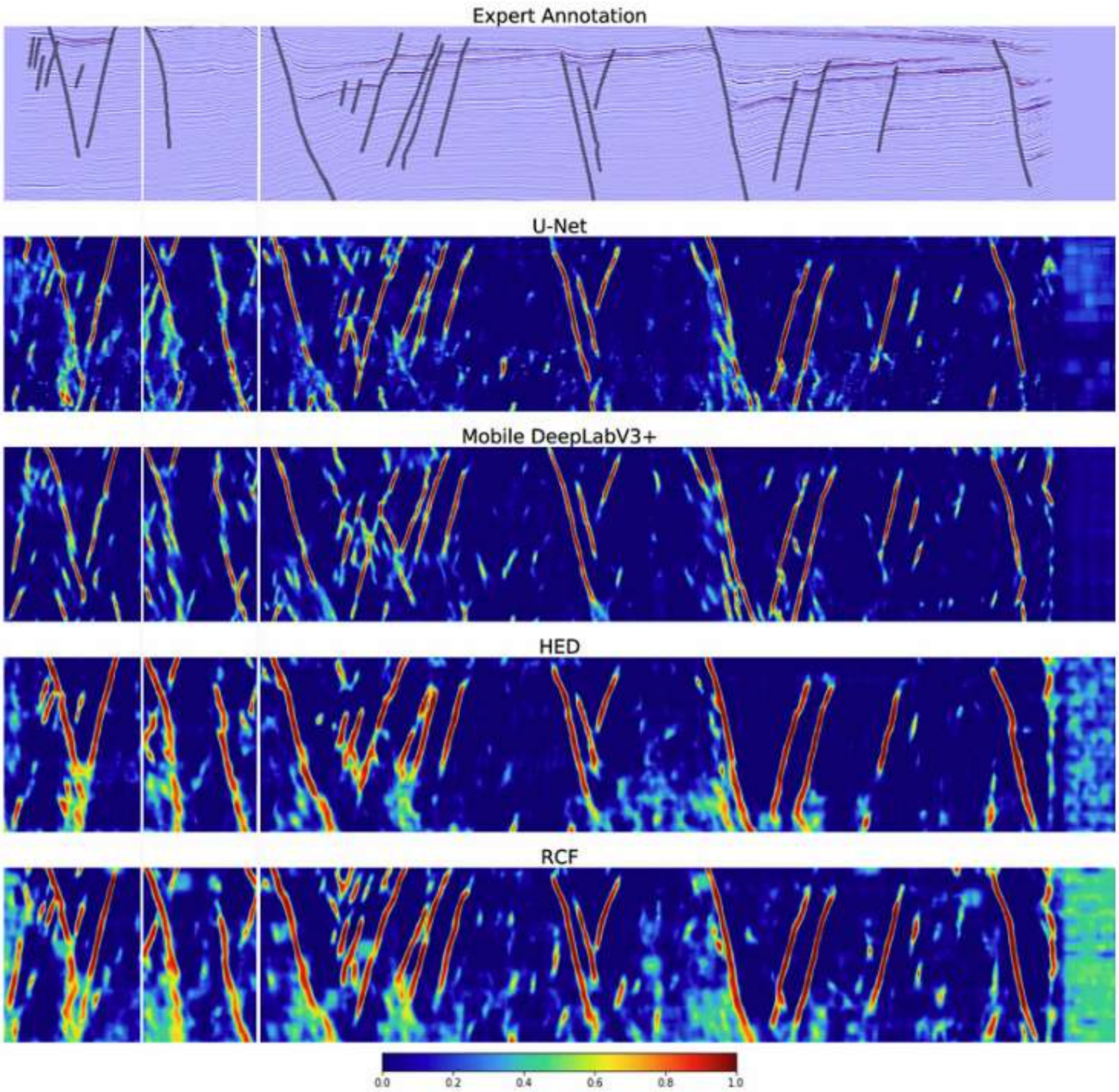

Figure 18 - A comparison of different networks architectures on a crossline of Thebe test set showing the fault probability predicted by each of the models. Extracted from An et al. (2021).

2. Seismic fault segmentation using deep learning-based applications

Fault mapping in seismic cubes is crucial for understanding subsurface structures, as faults often play a key role in fluid migration, hydrocarbon trapping, and geohazard assessment. This is particularly significant in the Brazilian pre-salt, where reservoirs are composed of highly heterogeneous carbonates beneath thick salt layers. These complex geological conditions pose significant imaging challenges while underscoring the need for detailed fault characterization to enhance reservoir management and optimize hydrocarbon exploration.

The advent of 3D seismic surveys has significantly advanced fault mapping by providing detailed images of large rock volumes and revealing complex fault networks. However, interpreting faults remains challenging because faults are not directly imaged in seismic data. Instead, they are inferred from discontinuities in continuous seismic reflections caused by changes in seismic impedance across rock layers. Manually digitization of these disrupted zones, where reflections are offset, is time-consuming and prone to subjectivity, adding further complexity to the task (Robein, 2010; Biondi et al., 2007).

Conventional fault interpretation from seismic reflection data relies on data quality and interpreter experience (Alcalde et al., 2017; Faleide et al., 2021; Gibson et al., 2012). Although fault mapping from high-quality seismic data is relatively objective, it remains time-consuming and repetitive. Interpreting a single dataset can take weeks to months (Gibson et al., 2012). Moreover, even high-quality seismic datasets often display signal disturbance zones, especially in regions with many faults. These disturbances can lead to poorly resolved discontinuities in seismic reflectors, resulting in imprecise fault locations or misinterpretation (Badley et al., 1991; Iacopini et al., 2016; Alcalde et al., 2019). Compounding the challenge, the uncertainty inherent in fault interpretation is often overlooked and remains difficult to quantify.

The significant growth in seismic data acquisition over the years has introduced challenges for oil and gas companies and research groups.

The rising demand for automatic and semi-automatic fault interpretation highlights the evolving needs of geologists and geophysicists, particularly in the oil and gas industry. Earlier studies primarily focused on developing and applying various derived volumes and attributes to enhance traditional fault interpretation workflows. These include dip/azimuth, coherence (Marfurt et al., 1999), curvature (Roberts, 2001), and similarity (Marfurt et al., 1998).

With advancements in computational power, many machine-assisted semi-automatic solutions have been proposed, utilizing simple feature analysis techniques, such as Ant Tracking (Pedersen et al. (2002)) and the Hough transform (Wang & AlRegib, 2014). However, due to variations in geological structures and data quality across datasets, these methods often require manual tuning through trial and error. Furthermore, these approaches rely on the subjective selection of one or a small set of features to guide fault interpretation, introducing potential biases and variability in results.

Tanaka et al. (2022) utilized faults as inputs for fracture modeling in Brazilian pre-salt. Fracture sets were mapped using conceptual relay ramp models and azimuth attributes derived indirectly from seismic coherence volumes. By leveraging faults to guide the stochastic modeling of fracture corridors, the study highlighted how fault architecture significantly influences fracture intensity and the preferential pathways for fluid flow.

In recent years, significant efforts has been dedicated to devoted to developing deep learning solutions for fault identification in seismic data. Among these, Wu et al. (2019a) serve as the leading reference in this area. While earlier studies (e.g., Huang et al., 2017; Zhao and Mukhopadhyay et al., 2018; Guo et al., 2018; Di et al., 2018; Guitton, 2018) and contemporaneous research (e.g., Pochet et al., 2019; Zhang et al., 2019; Montaron et al., 2019; Cunha et al., 2019) contributed to the field, the open-source nature of Wu et al.'s study has established it as a benchmark for fault detection using deep learning. Subsequently research explored alternative approaches to address this complex task. For example, An et al. (2021), Dou et al. (2021a), and Dou et al. (2021b) proposed CNNs with specialized architectures and loss functions tailored for edge detection and noise reduction, moving beyond the conventional pixel classification paradigm.. Meanwhile, Guo et al. (2020) proposed a CNN model capable of identifying both horizons and faults, arguing that this approach would produce fault estimates more consistent with geological structure.

Some studies have shifted focus from deep learning algorithms and network architectures to the underlying data itself. Otchere et al. (2022), for example, utilized a pre-trained CNN to predict fault locations in preconditioned seismic data. This approach effectively tailored the appearance of application data to align with the training dataset, though it often fell short of fully representing the complex characteristics of real seismic data. Jing et al. (2022) adopted a different strategy by enhancing the realism of the training dataset. Using the same U-Net architecture proposed by Wu et al. (2019a), they introduced slight modifications to the forward seismic modeling process, improving the alignment between synthetic training data and real-world seismic scenarios.

In this study, we propose deep learning approaches to address the challenges of fault interpretation in pre-salt seismic data. We begin by reviewing conventional seismic interpretation techniques alongside state-of-the-art deep learning-based methods. Next, we introduce a workflow for generating synthetic training data. Following this, we describe the fundamentals of convolutional neural networks (CNNs), detailing their training processes. We then analyze and evaluate the performance of these models. Finally, we demonstrate the application of our approach on real field examples and provide a qualitative discussion of their advantages and implications.

2.1. Theory and methodology

2.1.1. Geometric seismic attributes

Seismic attributes are essential tools for interpreting and analyzing seismic data, especially in structural and stratigraphic investigations. Geometric attributes, derived from the spatial and geometric properties of seismic events, offer valuable insights into subsurface characteristics that are often challenging to identify using traditional amplitude-based attributes alone.The most commonly used geometric attributes include coherence, dip, and curvature. These attributes provide critical insights into subsurface, revealing features such as faults, folds, fractures, and depositional patterns. Such information is essential for seismic fault interpretation and reservoir characterization.

Marfurt et al. (1998) introduced a semblance-based approach to measure coherence between adjacent seismic traces. They used the attribute to identify structural and stratigraphic discontinuities, such as faults. Semblance discontinuity measures the variance between a set of traces around a mean trace, normalized by average energy (Barnes, 2016).

A significant drawback of basic implementations of the coherence attribute is their inaccuracy on tilted reflectors, as the algorithm does not account for local tilt. Without incorporating dip-steering techniques (Tingdahl & De Groot, 2003), the attribute will inaccurately mark tilted reflectors as discontinuous zones.

The dip attribute is crucial for various geological studies, particularly in structural and stratigraphic interpretation. However, it is important to recognize that a seismic reflection is only an image—an imperfect representation of the actual geological reflector. Consequently, any property derived from this image will reflect the true geological characteristics of the subsurface only to the extent that the image quality permits. For dip estimation, factors such as low signal-to-noise ratios and limited seismic resolution (both vertical and lateral) can significantly affect accuracy.

The method used for dip estimation in this study is the Gradient Structure Tensor (GST) method, initially proposed by Bakker et al. (1999) and Randen et al. (2000). This approach aims to identify the principal directions of amplitude variation in the seismic data, where one direction represents the maximum variation, normal to the reflection plane, while the other two exhibit minimal variation and align with the reflection. In their approach, the authors employed Principal Component Analysis (PCA) to construct a 3x3 tensor from pre-calculated amplitude derivatives. These derivatives are estimated by convolving the seismic data with the derivative of a Gaussian filter. Curvature attributes are used to quantify the bending of seismic reflectors in the subsurface and are categorized into different types. Staples et al. (2013) and Chopra and Marfurt (2015) established correlations between the most positive curvatures (k1) and the most negative curvatures (k2) in relation to fractured zones and fracture density/intensity. These curvature types reveal subtle variations in the geometry of geological surfaces, which are crucial for identifying specific patterns. Long-wavelength curvature captures the overall deformation associated with significant geological features, such as horsts, grabens, and fault zones, with a considerable throw. In contrast, short-wavelength curvature provides detailed delineation of fault features, even when their displacements are below seismic resolution. In carbonate formations, Bravo and Aldana (2010) demonstrated the potential of curvature attributes to identify subseismic faults and fractured zones at the wellbore scale. Hunt et al. (2018) explored various window sizes and post-filtering techniques, emphasizing the importance of aligning parameters with the depth, scale, and geometry of the targets. Oliveira Neto et al. (2023) presented seismic curvature analysis workflows applied to pre-salt carbonates, demonstrating and analyzing different parameterizations that best fit both qualitatively and quantitatively.

2.1.2. Synthetic dataset generation

The workflow employed to generate synthetic seismic and fault images, as detailed by Wu and Hale (2016), consists of several key steps. First, a 1D horizontal reflectivity model is created, incorporating a sequence of random values within a specified range. Next, folding structures are introduced into the reflectivity model through vertical shearing. First, into the model, after which the data is convolved a Ricker wavelet to produce a 3D seismic image.

One potential limitation of applying this methodology to our case is the use of the 1D convolutional model for direct seismic modeling. While this approach is effective for many seismic datasets, it may not be suitable for datasets with a broader frequency spectrum or those affected by illumination issues (Figure 19).

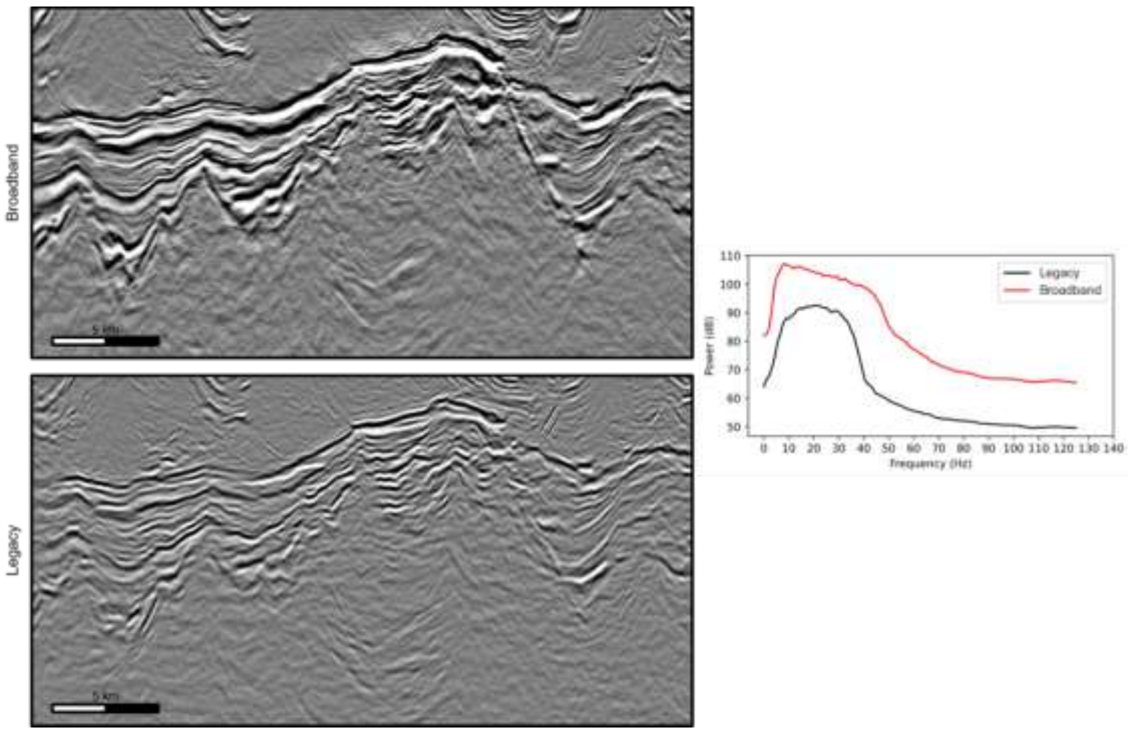

Figure 19 - Difference in frequency spectrum between seismic data broadband and legacy.

To address this issue, we draw on the workflows proposed by Wu et al. (2020) and Vizeu et al. (2022), but with modifications that enhance the dataset's suitability for pre-salt seismic applications. We commence by creating cross-sections with random pseudo-RGTs, introducing normal faulting using the methodology proposed by Wu et al., 2019. We then perform FFT-MA for stochastic simulations of acoustic impedance and conducting forward modeling convolving the reflectivity model with several Point-Spread Function (PSF), as proposed by Lecomte, (2003) and Jing et al., (2023). This modification aims to enhance the realism of the training dataset. Unlike the conventional 1D convolution with a given wavelet and reflectivity model, we employ a fast ray-based approach based on point-spread functions. This method is recognized for producing synthetic seismic data closely resembling accurate PSDM seismic data, including Reverse Time Migration (RTM) images (Jensen et al., 2021).

Jing et al. (2023) explored the impact of the direct seismic modeling method employed to create synthetic seismic data on fault prediction in real seismic datasets. Their findings indicated that the network trained with direct convolutional modeling based on the point-spread function (PSF) performed better in fault detection than the one trained with the 1D convolution-based approach.

We generated 400 pairs of 3D synthetic datasets, each with a size of 128x128x128 (Figure 20). Although a larger number of data pairs could have been generated, we chose this amount to facilitate comparisons with previous studies from other authors. To further enhance the diversity of the dataset, we applied data augmentation techniques, including rotations of 90°, 180°, and 270°.

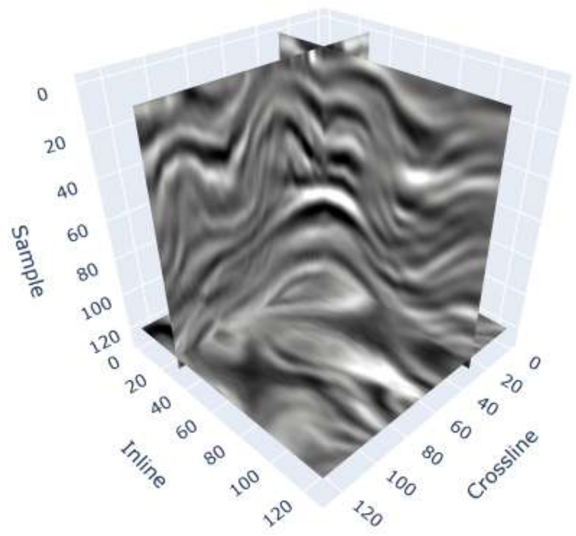

Figure 20 - 3D Synthetic data using PSF convolution.

2.1.3. CNN for fault segmentation

Machine learning is a key subfield of artificial intelligence that focuses on developing algorithms and models capable of autonomously acquiring knowledge and making predictions or decisions without explicit programming. It utilizes statistical techniques and data to train computational systems, enabling them to perform specific tasks and generate accurate predictions. A prominent subset of machine learning, deep learning, is inspired by the structure and functionality of the human brain, enabling more advanced and complex models for a variety of applications (LeCun et al., 2015).

Deep learning is a specialized domain focused on leveraging large models to tackle complex problems. It is particularly suited for tasks that involve extensive datasets and high-performance computing (HPC), as more intricate architectures demand significant computational power to process vast amounts of data and capture complex relationships between variables. A key example of these architectures is deep neural networks. These networks consist of multiple interconnected layers of artificial neurons, designed to emulate the cognitive processes observed in the human brain, enabling them to learn and solve a wide range of problems. Convolutional neural networks (CNNs) are deep learning algorithms commonly used for image recognition, classification, and segmentation (LeCun et al., 2015). CNNs are composed of several convolutional and pooling layers, followed by one or more fully connected layers that make predictions based on the features extracted. Unlike traditional neural networks, where each neuron in the input layer is connected to every neuron in the hidden layers, CNNs use a localized approach. In a CNN, only a small region of neurons from the input layer connects to neurons in the hidden layers, allowing the network to efficiently capture spatial hierarchies in data.

Image segmentation divides an image into multiple segments or regions, each corresponding to a specific object or part of the image. One type of image segmentation is semantic segmentation, which assigns a class label to each pixel in the image (pixel-by-pixel classification). A widely used architecture for this task is U-Net, a convolutional neural network (CNN) introduced by Ronneberger et al. (2015). U-Net has become a popular tool for semantic segmentation, particularly in applications with limited training data, such as biomedical image segmentation, where datasets are often small.

2.1.3.1. U-Net architecture

The U-Net architecture consists of three main components: the encoder, the decoder, and skip connections. The encoder is responsible for extracting and locating features in an image, which are used to predict the presence of objects in the image. It creates a lower-dimensional representation of the input image by extracting features using convolution and pooling layers. Thus, the encoder gradually reduces the spatial resolution of the input image while increasing the number of channels, allowing it to capture high-level features. However, the encoder's output lacks location information, which is essential for segmentation. In contrast, the decoder reconstructs an image from the compact representation using a deconvolution layer, while reducing the number of channels. Skip connections pass information from earlier convolution layers to the deconvolution layers, enabling the network to retain information about the location of features in the image that would otherwise be lost during downsampling. The key to U-Net's success lies in this part. The skip connections allow for precise segmentations with fewer data, making it particularly useful for small datasets, such as medical image segmentation datasets, in contrast to autoencoder architectures, which require immense amounts of data to accurately reconstruct images from compacted representations.

Since fault detection is approached as a binary segmentation problem, we implemented a network based on the simplified U-Net architecture proposed by Wu et al. (2019). In the contracting path (left side), each step consists of two $3 \times 3 \times 3$ convolutional layers, followed by a ReLU activation and a $2 \times 2 \times 2$ maxpooling operation with a stride of 2 for downsampling. Each step in the expansive path (right side) contains a 2 × 2 × 2 transposed convolution operation, a concatenation with the patterns from the contracting path, and two 3 × 3 × 3 convolutional layers followed by a ReLU activation (Figure 21).

To address the complexity of the problem, we enhanced the network's depth by adding an extra layer, resulting in a five-layer architecture. We opted to incorporate a transposed convolutional layer, also known as a deconvolutional layer, which upscales the input data to a higher spatial resolution. Unlike regular convolution, this layer spreads the input data over a kernel to produce an expanded output. Although it does not exactly reverse convolution, it restores the original dimensions. This technique is used in tasks such as image generation, super-resolution, and segmentation, where upsampling is essential. The transposed convolution operation is implemented using the Conv3DTranspose function defined in Keras (Chollet, 2015). We experimented with batch normalization and the addition of dropout layers, but these adjustments did not lead to any improvement in the results. The final output layer is a 1 × 1 × 1 convolutional layer with a sigmoid activation.

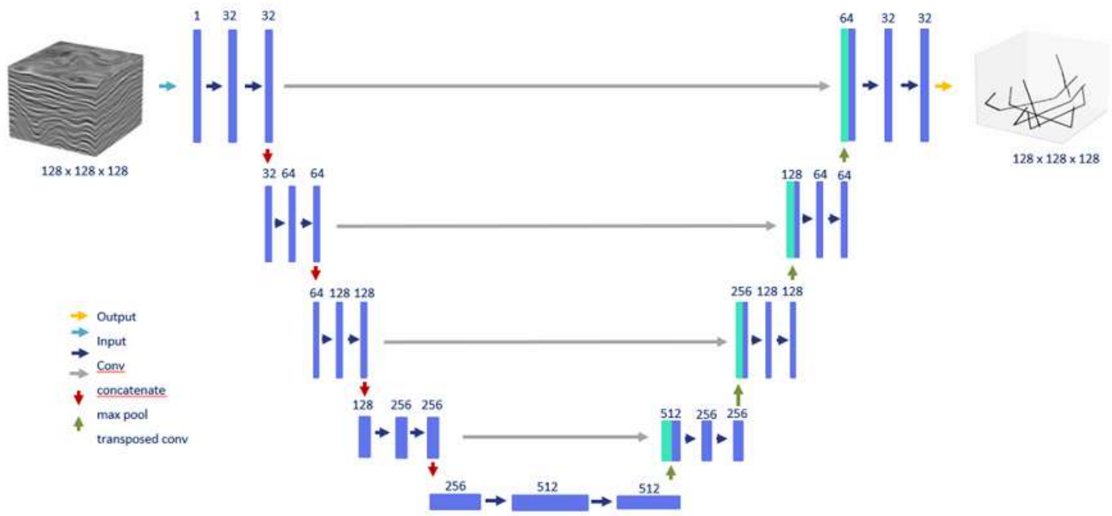

Figure 21 - U-Net network architecture for fault segmentation.

2.1.3.2. Balanced-Cross Entropy

Initially, we used Binary Cross-Entropy as the loss function, given its popularity for binary segmentation tasks. While the network achieved satisfactory accuracy, we observed that the predictions lacked continuity and consistent probability values. To address this, we switched to the Balanced Cross-Entropy loss function proposed by Wu et al. (2019), which improved the quality of the predictions:

$$L = -\beta \sum_{i=0}^{i=N} y_i \log(p_i) - (1 - \beta) \sum_{i=0}^{i=N} (1 - y_i) log(1 - p_i) \quad (26)$$

This adjustment addresses class imbalance, preventing the network from being trained or converged to predict only zeros.

2.1.3.3. Training and testing

We trained the model with a batch size of 32, using the Adam optimizer (Kingma and Ba, 2014) for parameter optimization and a learning rate of 0.001 for 200 epochs. The training and test datasets contain 360 and 40 labeled 3D synthetic seismic amplitude data, respectively. To evaluate the network's performance, we calculated the loss and accuracy on both training and validation data throughout the training process. Figure 22 illustrates the variations of these metrics over the epochs and Figure 23 displays the model's predictions for slice 64 of the test data. Training, testing, and application were performed on an NVIDIA RTX A5000 GPU.

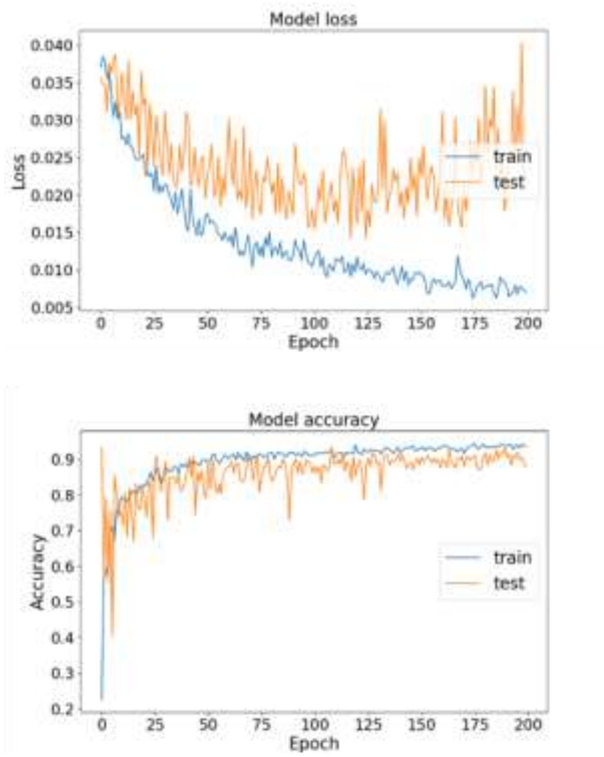

Figure 22 - Loss function and accuracy curves for training and validation.

The accuracy curve for both training and validation gradually increases, exceeding 90%, while the loss converges to stable values. However, there are noticeable gaps between the loss and accuracy curves, with these differences being more pronounced in the validation set compared to the training set.

According to Jing et al. (2023), one possible explanation for these gaps is the variability in fault characteristics in data synthesized with PSF convolution, influenced by dominant frequencies and velocities. This variability could result in differences in the network's predictions between the training and validation sets.

The network performs well in detecting faults with sharp edges and large displacements. However, it partially and even completely misses faults with smaller displacements or some complex features.

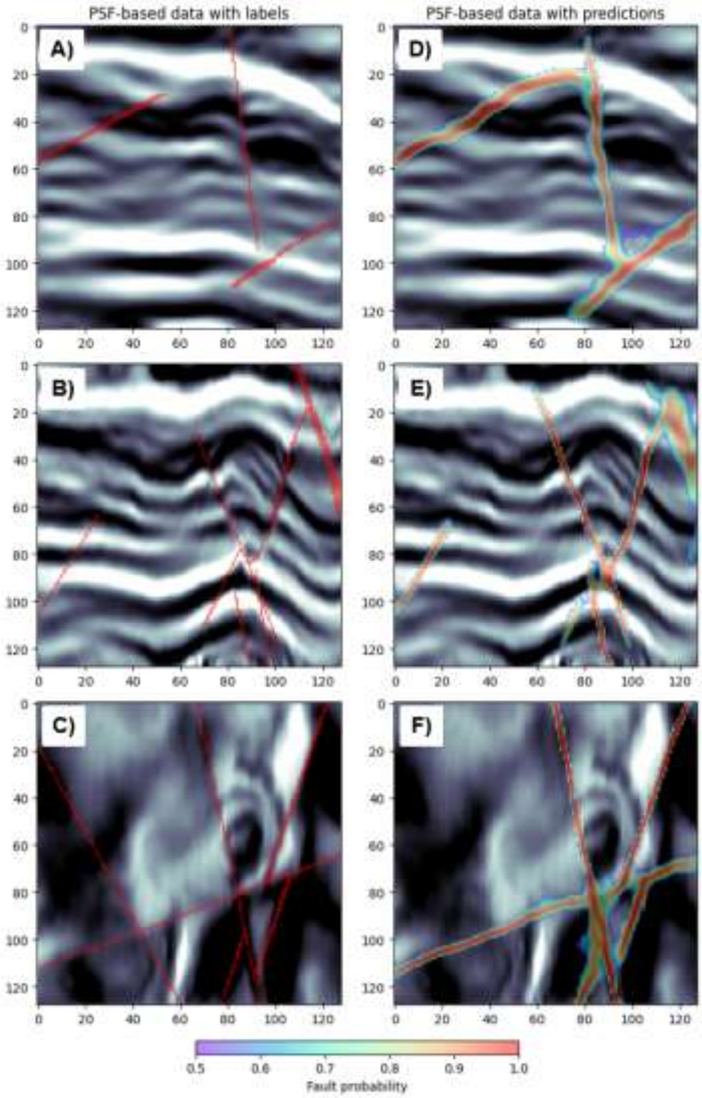

Figure 23 - Fault probability on the synthetic seismic image overlaid with the corresponding true label in A) inline; B) crossline; and C) depth slice. In (D-F) we have the prediction from the CNN, respectively.

2.2. Application

2.2.1. Geological Setting

Santos Basin, the largest offshore basin in Brazil, stretches from the southern coast of the State of Rio de Janeiro to the northern reaches of the State of Santa Catarina. Situated between the parallels 230 and 280 of south latitude, it lies in the southeastern expanse of the Brazilian continental margin. Bounded to the north by the Cabo Frio high (which demarcates the limit with Campos Basin) and to the south by the Florianopolis high (separating it from the Pelotas Basin), the Santos Basin encompasses an area of approximately 350,000 square kilometres, with bathymetric depths reaching up to 3km.

The Búzios field is one of the main producers in the Brazilian pre-salt (Figure 24). The pre-salt carbonate reservoirs were deposited beneath a thick salt layer at great depths (approximately 5,000 meters), posing a challenge for seismic imaging and illumination. The application data for this work comes from an ocean-bottom node (OBN) seismic acquisition with a broadband spectrum, capturing geological information at both lower and higher frequencies compared to older data, which had a narrower bandwidth.

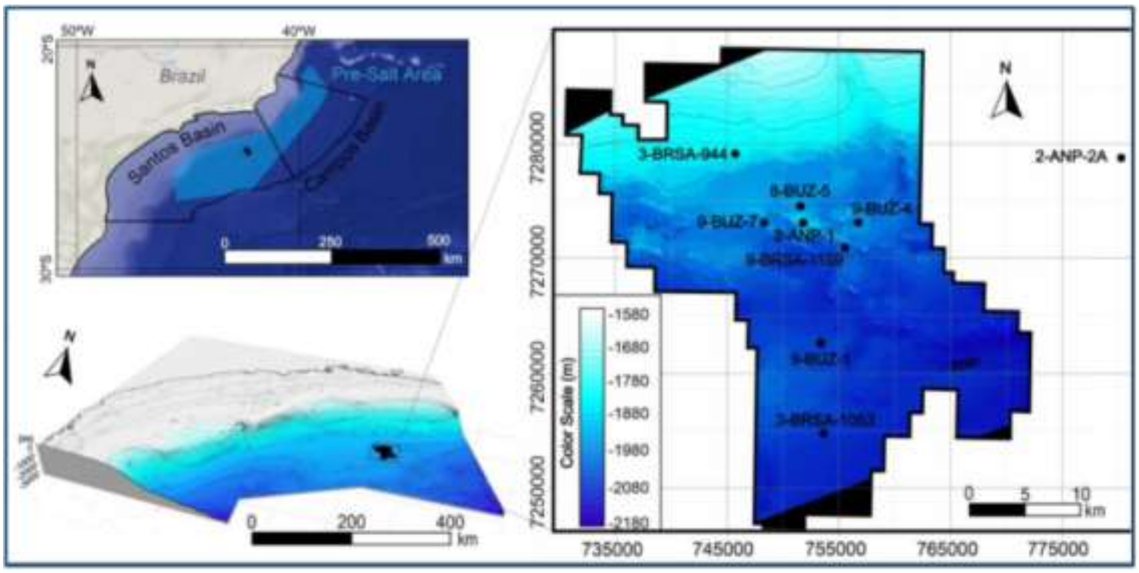

Figure 24 - Búzios field location.

2.2.2. Seismic data preconditioning

Although the synthetic data visually resembles our real application data, achieving better performance requires aligning the characteristics of the application data with the training dataset, which generally cannot fully represent the true aspects of real seismic data. Many techniques are often used to improve the resolution of the fault in the seismic. These methods often rely on filters that serve as fault enhancement attributes.

To achieve this, we applied several filtering processes and plugins available in OpendTect. Initially, we used a pre-trained model (3D U-Net) from AkerBP (Lundin-Geolab), designed to reduce random noise and optimize amplitude-frequency content. Next, we applied the Dip-Steered Median Filter to enhance laterally continuous seismic events, filtering along the structural dip of reflectors. Although effective at reducing noise, these smoothing filters tend to blur edges and compromise the fidelity of key features. To address this, we applied to the Edge Preserving Smoothing Filter (EPS), aiming to balance noise reduction with the preservation of detailed geological structures. It is a type of Recursive Gaussian Filter (e.g., Deriche, 1993; Hale, 2002) that considers the information of Fault Likelihood volume ($1 - coherence^8$) (Hale, 2013). The output resembles results from the literature that used LoG (Laplacian of Gaussian) operators or Kuwahara filters to enhance faults in seismic images (Chopra and Marfurt, 2017).

However, the standard EPS filter, which uses coherence seismic attribute information, has a drawback: while it highlights discontinuities, it can distort fault shapes due to the nature of these discontinuities. To overcome this challenge, we applied a workflow that we called Bootstrap (Nilo et al., 2024). In this approach, we used the fault probability predicted by the CNN as input to estimate the Fault Likelihood attribute, now containing dip and strike information. By incorporating this attribute as a guide for the EPS filter, we enhanced its performance, enabling a more effective application of the network (Figure 25).

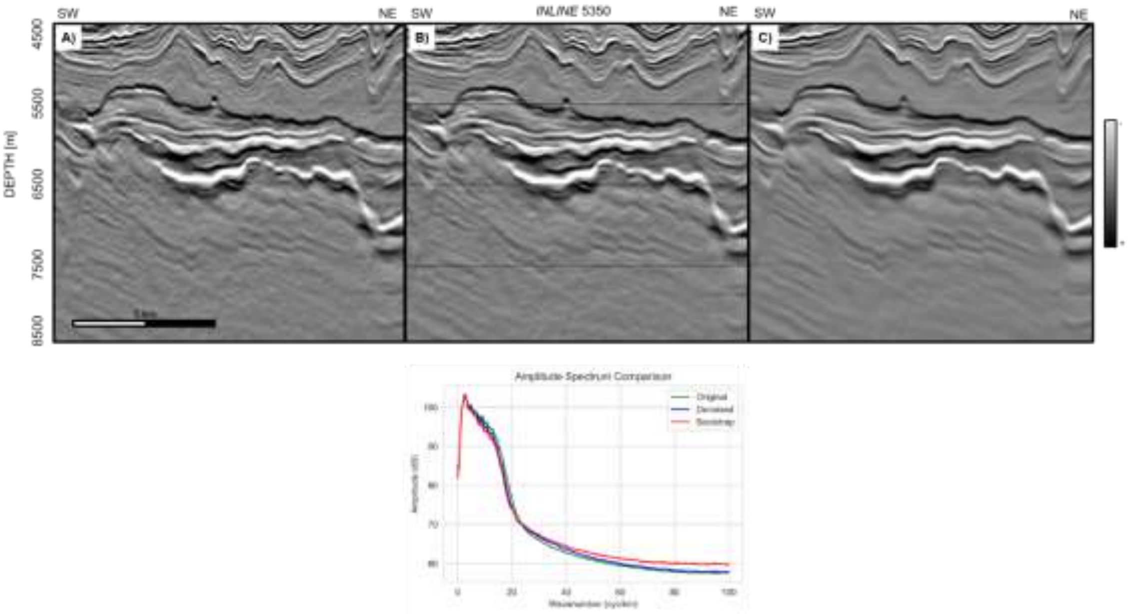

Figure 25 - In A) we have the unfiltered seismic section; B) Pre-trained CNN for noise removal; C) "Bootstrap" workflow. Below thoses sections show the amplitude spectra from all three data.

2.2.3. Fault probability

In qualitatively evaluating the network's performance on the field example,, we noticed that successfully captured various fault trends. The network was able to segment discontinuities with small to medium displacements. A considerable number of faults with relatively small displacements are present within the 3D seismic volume, and the network accurately predicted them in certain regions (Figure 26). However, it is important to note that the network also experienced numerous artifacts, particularly when segmenting discontinuities associated with deviations in layer dips, which negatively impacted the overall efficiency of the model.

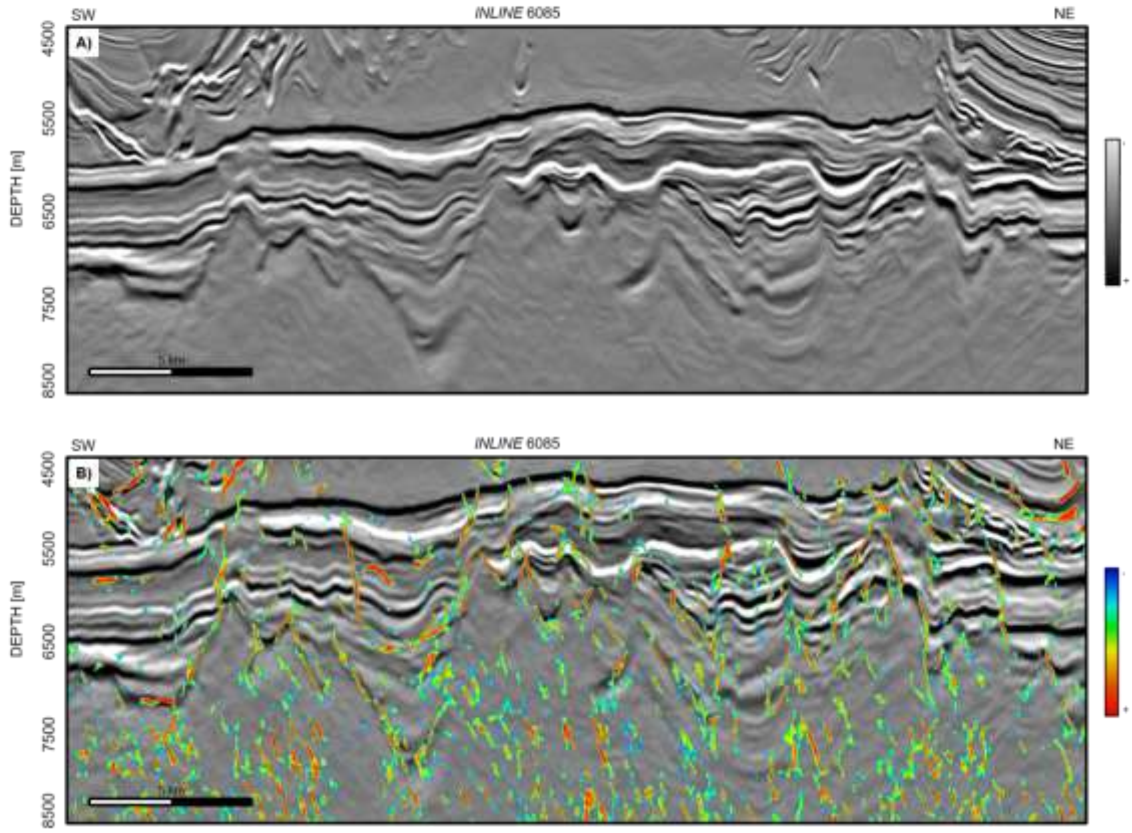

Figure 26 - In A) inline seismic section with noise removal and stratigraphic surfaces; in B) fault probability extracted in the Búzios volume after noise removal. The scale ranges from 0.5 to 1.0, where the warmer colors (red) indicate high probability of discontinuities, while the cooler colors (blue) indicate low probability.

2.3. Discussion

2.3.1. A comparison with conventional methods

Although we do not directly interpret the result, traditional structural curvature extractions are calculated from dip estimates through lateral scanning of seismic events. These extractions are influenced by parameter configurations, seismic frequency, and data quality (Figure 27a).

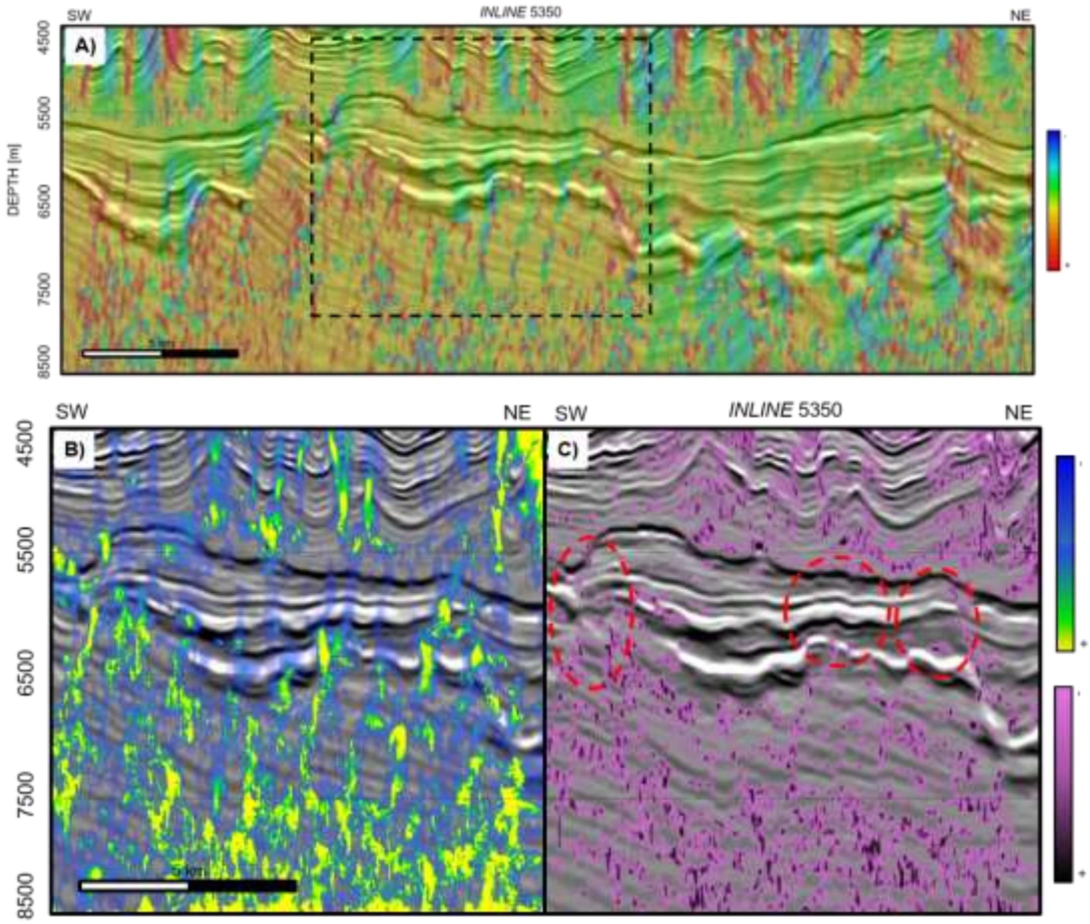

Figure 27 - In A) dip volume extracted and applied to the inline seismic section 5350. Seismic panel of the area highlighted in A) with the evaluated geometric attributes B) k1 curvature; C) coherence. The red dashed circles indicate areas where coherence failed to define seismic discontinuities interpreted as faults or deformed areas prone to the presence of fractures.

We sought to parameterize curvature to highlight subtle small-scale features such, as subseismic faults and fractured zones by evaluating it qualitatively and comparing it with the coherence attribute. The coherence attribute highlights only the most prominent seismic discontinuities, typically associated with clearly visible displacements in seismic events. However, it fails to capture other discontinuity features, such as faults with throws near the limit of seismic resolution, amplitude attenuation, or the curvature of seismic events (Figure 27b-c).

Accurate detection of these faults remains challenging. However, when compared to conventional methods, the reduction in artifacts is substantial, and the predictions are more reliable from a qualitative perspective (Figure 28).

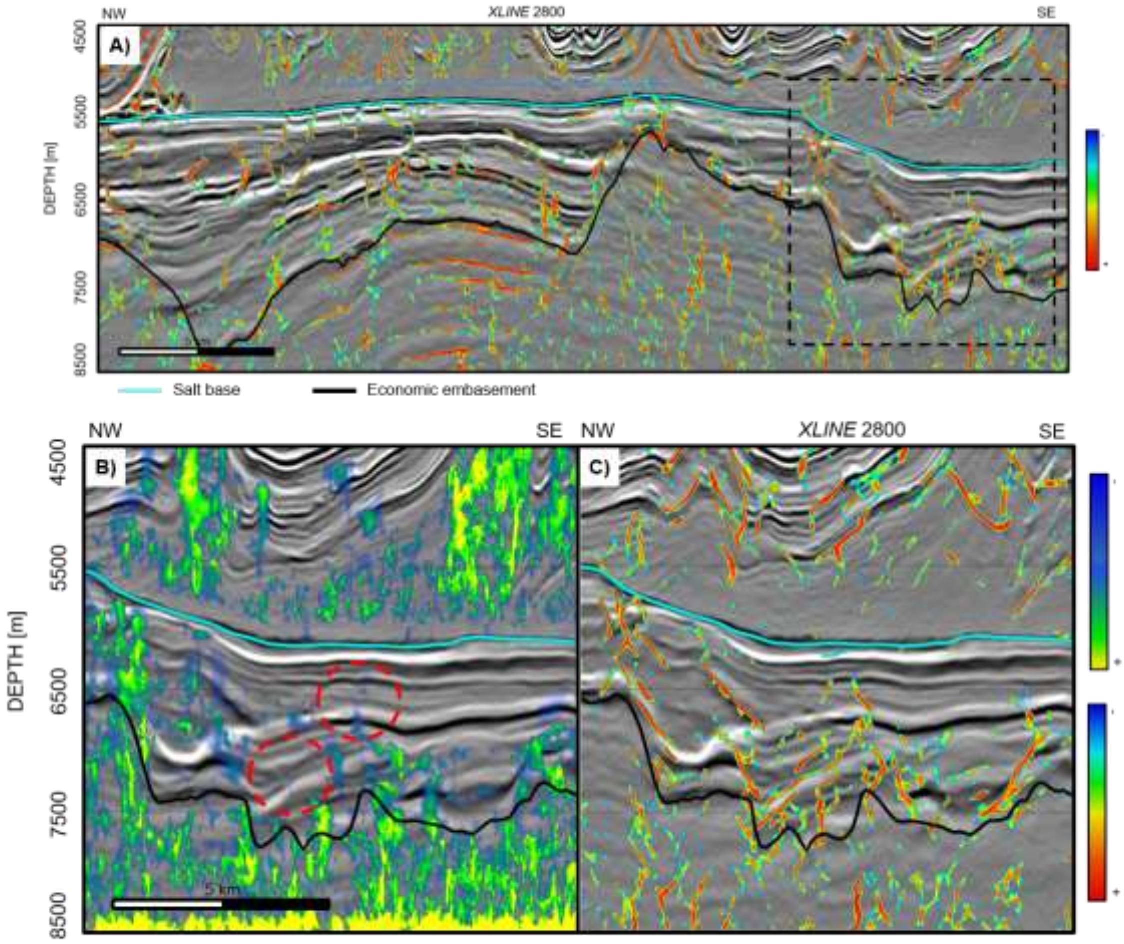

Figure 28 - In A) crossline seismic section with noise removal and stratigraphic surfaces overlaid with fault probability extracted in the Búzios volume after noise removal. The scale ranges from 0.5 to 1.0, where the warmer colors (red) indicate high probability of discontinuities, while the cooler colors (blue) indicate low probability. In the seismic panel of the area highlighted in A) we have B) k1 curvature and C) fault probability predicted by the network. The red dashed circles indicate areas where the network performed qualitatively better, capturing discontinuities that the attribute was not able to identify or has a low value on the scale.

2.3.2. The impact of the preconditioning the seismic data

After preconditioning, there is a significant improvement even when compared to noise filtering alone (Figure 28a), since the fault prediction is more continuous and with fewer artifacts (Figure 29). However, as with any filtering process, there is a risk of losing valuable information. In this case, the filter suppresses small-scale features related to subseismic faults.

Finally, for better visualization, we extracted the fault probability volume along the seismic horizon corresponding to the salt base on the Z-axis (Figure 30). This approach allows for a qualitative analysis of the impact of the Bootstrap workflow on the network's predictions, facilitating the delineation of more distinct fault segments and enhancing the overall performance of the network.

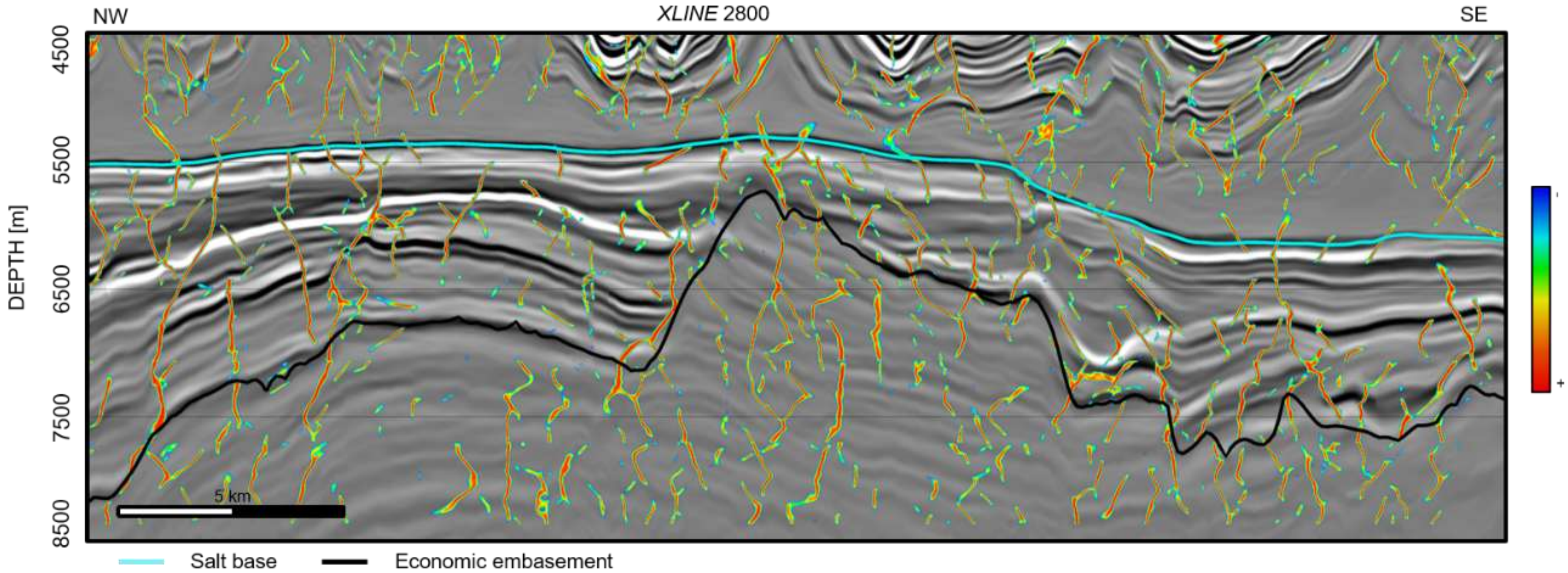

Figure 29 - Fault probability extracted in the Búzios volume after applying the Bootstrap workflow. The scale ranges from 0.5 to 1.0, where the warmer colors (red) indicate a high probability of discontinuities, while the colder colors (blue) indicate a low probability.

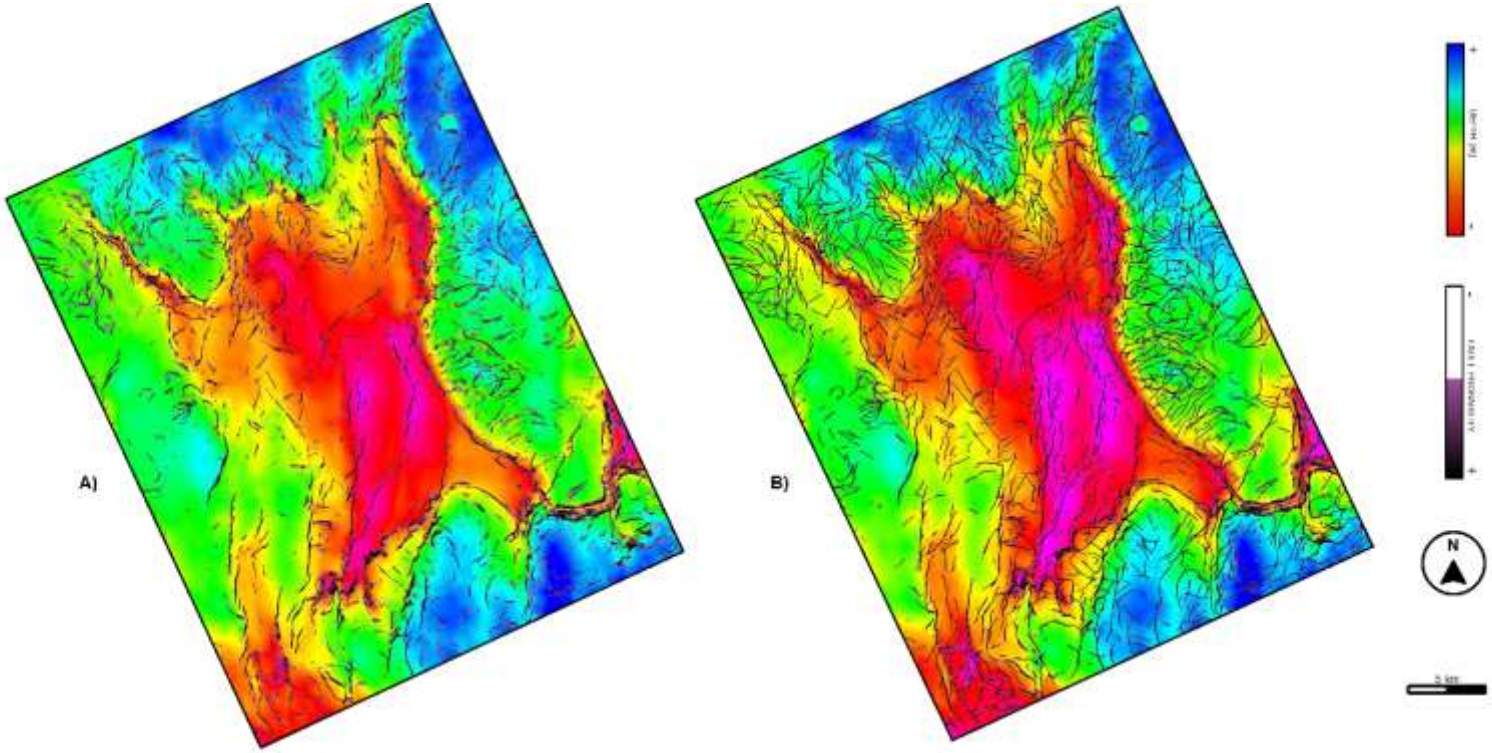

Figure 30 - Salt base seismic surface of Buzios field with the fault probability overlayed. In A) we have applied to denoised volume; B) after the Bootstrap preconditioning workflow. The rainbow colorbar indicates that shallowest depths are related to warmer colors (red) while deepest are related to cold colors (blue). The fault probability shows lower values in transparency and higher values ranging from purple to black, with a minimum value of 0.5 and a maximum of 1. Preconditioning produced some significant improvements in U-Net fault detection since it shows a more detailed definition of minor features related to sub-seismic faults and fractured zones as we can see both at shallow and deep depths.

2.4. Conclusions

We explored the application of deep learning techniques for seismic fault interpretation in the Búzios Field within the Brazilian pre-salt region. The workflow for synthetic seismic data generation, using point-spread function (PSF) convolution, created a realistic training dataset that accurately reflected the broadband characteristics of pre-salt seismic data. This approach ensured that the network was exposed to representative geological scenarios during training, enhancing its ability to generalize effectively. We trained a 3D U-Net model successfully to capture prominent fault trends and small-to-medium displacement discontinuities in the Búzios field. In addition, the preconditioning workflow significantly improved fault prediction continuity and minimized artifacts. By incorporating fault probability as a guide for edge-preserving smoothing, the workflow balanced noise reduction and feature preservation, producing cleaner and more interpretable outputs. Finally, we demonstrated the potential of modern machine learning methods to overcome the challenges inherent in traditional interpretation workflows.

3. References

Alcalde, J., Bond, C. E., Johnson, G., Ellis, J. F., & Butler, R. W. (2017). Impact of seismic image quality on fault interpretation uncertainty. GSA Today.

Alcalde, J., Bond, C. E., Johnson, G., Kloppenburg, A., Ferrer, O., Bell, R., & Ayarza, P. (2019). Fault interpretation in seismic reflection data: an experiment analysing the impact of conceptual model anchoring and vertical exaggeration. Solid earth, 10(5), 1651-1662.

Aminian, K., Ameri, S., 2005. Application of artificial neural networks for reservoir characterization with limited data. Journal of Petroleum Science and Engineering, 49(3-4), 212-222, https://doi.org/10.1016/j.petrol.2005.05.007.

An, Y. and Dong, R. [2023] Understanding the Effect of Different Prior Knowledge on CNN Fault Interpreter. IEEE Access, 11, 15058–15068.

An, Y., Guo, J., Ye, Q., Childs, C., Walsh, J. and Dong, R. [2021] Deep convolutional neural network for automatic fault recognition from 3D seismic datasets. Computers Geosciences, 153, 104776.

Aqrawi, A. A. M., & Boe, T. (2011). Improved fault segmentation using a multiattribute approach. First Break, 29(9), 39-47. DOI: https://doi.org/10.3997/1365-2397.29.9.70112

Badley, M. E., Freeman, B., Roberts, A. M., Thatcher, J. S., Walsh, J., Watterson, J., & Yielding, G. (1991). Fault Interpretation During Seismic Interpretation and Reservoir Evaluation: Fractured Reservoirs: Origin, Description, Evaluation.

Bahorich, M., Farmer, S., 1995. 3-D seismic discontinuity for faults and stratigraphic features: The coherence cube. The Leading Edge 14, 1053–1058. https://doi.org/10.1190/1.1437077

Bakker P, van Vliet LJ, Verbeek PW (1999) Edge preserving orientation adaptive filtering. Proceedings. 1999 IEEE Comput. Soc. Conf. Comput. Vis. Pattern Recognit. (Cat. No PR00149), Comput. Vis. Pattern Recognition, 1999. IEEE Comput. Soc. Conf. on. VO - 1 535-540. https://doi.org/10.1109/CVPR.1999.786989

Barnes, A. E. (Ed.). (2016). Handbook of poststack seismic attributes. Society of Exploration Geophysicists.

Bhattacharya, S., & Verma, S. (2019). Application of volumetric seismic attributes for complex fault network characterization on the North Slope, Alaska. Journal of Natural Gas Science and Engineering, 65, 56-67.

Bravo, L., Aldana, M., 2010. Volume curvature attributes to identify subtle faults and fractures in carbonate reservoirs: Cimarrona formation, middle Magdalena valley basin, Colombia. SEG Technical Program Expanded Abstracts 2010 2231–2235. https://doi.org/10.1190/1.3513293

Chollet, F., & others. (2015). Keras. GitHub. Retrieved from https://github.com/fchollet/keras

Chopra, S., & Marfurt, K. J. (2005). Seismic attributes—A historical perspective. Geophysics, 70(5), 3SO-28SO.

Chopra, S., Marfurt, K.J., 2007. Volumetric curvature attributes adding value to 3D seismic data interpretation. Society of Exploration Geophysicists - 77th SEG International Exposition and Annual Meeting, SEG 2007 851–855

Chopra, S., 2009. Interpreting fractures through 3D seismic discontinuity attributes and their visualization., CSEG Recorder

Chopra, S., & Marfurt, K. J. (2015, October). Choice of mother wavelets in CWT spectral decomposition. In *SEG International Exposition and Annual Meeting* (pp. SEG-2015). SEG.

Chopra, S., & Marfurt, K. J. (2017). Volumetric fault image enhancement—Some applications. Interpretation, 5(2), T151-T161.

Correa, R.S.M., Pereira, C.E.L., Cruz, F.A.S., Lisboa, S.N.D., Junior, M.P.A., Carvalho, B.R.B.M., Souza, V.H.P., Rocha, C.H.A., Araujo, F.G., 2019. Integrated Seismic-Log-Core-Test Fracture Characterization, Barra Velha Formation, Pre-salt of Santos Basin. Search and Discovery. https://doi.org/10.1306/42425Correa2019

Cunha, A., Pochet, A., Lopes, H., Gattass, M., 2019. Seismic fault detection in real data using Transfer Learning from a Convolutional Neural Network pre- trained with synthetic seismic data. Computers and Geosciences 104344. https://doi.org/10.1016/j.cageo.2019.104344

Deriche, R., 1993. Recursively implementating the Gaussian and its derivatives. Rapports de Recherche INRIA 24.

Di, H., Shafiq, M., AlRegib, G., 2018. Patch-level MLP classification for improved fault detection. SEG Technical Program Expanded Abstracts 2211–2215. https://doi.org/10.1190/segam2018-2996921.1

Dou, Y., Li, K., Zhu, J., Li, X., Xi, Y., 2021. Attention-Based 3-D Seismic Fault Segmentation Training by a Few 2-D Slice Labels. IEEE Transactions on Geoscience and Remote Sensing 60, 1–15. https://doi.org/10.1109/TGRS.2021.3113676

Dou, Y.T. of 3D S.I.F.S.N. under S.L. by W.A.A., Li, K., Zhu, J., Li, T., Tan, S., Huang, Z., 2021. Efficient Training of 3D Seismic Image Fault Segmentation Network under Sparse Labels by Weakening Anomaly Annotation. 1–12.

Esmaeilzadeh, S., Afshari, A., Motafakkerfard, R., 2013. Integrating Artificial Neural Networks Technique and Geostatistical Approaches for 3D Geological Reservoir Porosity Modeling with an Example from One of Iran's Oil Fields. Petroleum science and technology, 31(11), 1175-1187, https://doi.org/10.1080/10916466.2010.540617.

Faleide, T.S., Braathen, A., Lecomte, I., Mulrooney, M.J., Midtkandal, I., Bugge, A.J., Planke, S., 2021. Impacts of seismic resolution on fault interpretation: Insights from seismic modelling. Tectonophysics 816, 229008. https://doi.org/10.1016/j.tecto.2021.229008

Ferreira, D. J. A., Dias, R.M., Lupinacci, W. M., 2021. Seismic Pattern Classification Integrated with Permo-Porosity Evaluation for Presalt Carbonates Reservoir Characterization in the Buzios Field, Brazil. Journal Petroleum Science and Engineering, 201, 108441, https://doi.org/10.1016/j.petrol.2021.108441.

Formigli, J. M., Pinto, A. C. C., Almeida, A. S., 2009. Santos Basin’s Presalt Reservoirs Development – The Way Ahead. Offshore Technology Conference, 4–7 May Houston, Texas

Gersztenkorn, A., & Marfurt, K. J. (1999). Eigenstructure-based coherence computations as an aid to 3-D structural and stratigraphic mapping. Geophysics, 64(5), 1468-1479.

Goodfellow, I., Bengio, Y., Courville, A., 2016. Deep Learning. Adaptive Computation and Machine Learning. Cambridge, Massachusetts: The MIT Press.

Guitton, A., Kaelin, B., & Biondi, B. (2007). Least-squares attenuation of reverse-time-migration artifacts. Geophysics, 72(1), S19-S23.

Guitton, A., 2018. 3D Convolutional Neural Networks for Fault Interpretation. 80th Conference + Exhibition. Copenhagen, Denmark.

Gunther, M.J., Marfurt, K.J., 2016. A Comparison of Alternative Volumetric Dip Computations. SEG International Exposition and 86th Annual Meeting. 2124–2127.

Guo, Y., Zhang, K., Kurt. J. M., 2010. Seismic Attribute Illumination of Woodford Shale Faults And Fractures, Arkoma Basin, OK. Paper presented at the 2010 SEG Annual Meeting, October, 2010, Denver, Colorado, USA. https://doi.org/10.1190/1.3513097.

Guo, B., Liu, L., Luo, Y., 2018. A new method for automatic seismic fault detection using convolutional neural network. SEG Technical Program Expanded Abstracts 1951–1955. https://doi.org/10.1190/segam2018-2995894.1

Hale, D., 2002. Recursive Gaussian Filters. Golden, CO. https://doi.org/10.1109/icpr.1998.711192 Hale, D., 2013. Methods to compute fault images, extract fault surfaces, and estimate fault throws from 3D seismic images. Geophysics 78. https://doi.org/10.1190/GEO2012-0331.1

Hale, D., 2013. Methods to compute fault images, extract fault surfaces, and estimate fault throws from 3D seismic images. Geophysics 78. https://doi.org/10.1190/GEO2012-0331.1

Hastie, T., Tibshirani, R., Friedman, J. H., 2009. The Elements of Statistical Learning: Data Mining, Inference, and Prediction. 2nd ed. Springer Series in Statistics. New York, NY: Springer.

Holdaway, K. R., Irving, D. H., 2017. Enhance Oil and Gas Exploration with Data-Driven Geophysical and Petrophysical Models. John Wiley & Sons

Hornik, K., Stinchcombe, M., White, H., 1990. Universal Approximation of an Unknown Mapping and Its Derivatives Using Multilayer Feedforward Networks. Neural Networks 3 (5): 551–60. https://doi.org/10.1016/0893-6080(90)90005-6.

Huang, L., Dong, X., Clee, T.E., 2017. A scalable deep learning platform for identifying geologic features from seismic attributes. Leading Edge 36, 249–256. https://doi.org/10.1190/tle36030249.1

Hunt, L., Beshry, B., Chopra, S., Webster, C., 2018. Determination of targetoriented parameters for computation of curvature attributes. Interpretation 6, 485–498. https://doi.org/10.1190/INT-2017-0202.1

Hughes, C., & Darby, B. (2021, September). Impact of fault displacement on syn-extensional carbonate deposition and excess permeability. In Second EAGE Conference on Pre-Salt Reservoir (Vol. 2021, No. 1, pp. 1-5). European Association of Geoscientists & Engineers.

Iacopini, D., Butler, R. W. H., Purves, S., McArdle, N., & De Freslon, N. (2016). Exploring the seismic expression of fault zones in 3D seismic volumes. Journal of Structural Geology, 89, 54-73.

Ioffe, S., Szegedy, C., 2015. Batch Normalization: Accelerating Deep Network Training by Reducing Internal Covariate Shift. In Proceedings of the 32nd International Conference on Machine Learning, edited by Francis Bach and David Blei, 37:448–56. Proceedings of Machine Learning Research. Lille, France: PMLR. http://proceedings.mlr.press/v37/ioffe15.html.

Jensen, K., 2021. Seismic modelling and deconvolution of prestack depth migrated images through ray-based Point-Spread Functions. University of Bergen.

Jesus, C., Olho Azul, M., Lupinacci, W. M., Machado, L., 2019. Multiattribute framework analysis for the identification of carbonate mounds in the Brazilian presalt zone: Interpretation, 7(2), 1–10, https://doi.org/10.1190/INT-2018-0004.1.

Jing, J., Yan, Z., Zhang, Z., Gu, H. and Han, B. [2023] Fault detection using a convolutional neural network trained with point-spread function-convolution-based samples. Geophysics, 88(1), IM1– IM14.

Kattah, S., Balabekov, Y., 2015. Seismic facies/geometries of the presalt limestone units and newly-identified exploration trends within the Santos and Campos basins, Brazil. SBGf, 288–293.

Kingma, D. P., & Ba, J. (2014). Adam: A method for stochastic optimization. arXiv preprint arXiv:1412.6980.

Lecomte, I., Gjøystdal, H. and Åsmund Drottning [2003] Simulated prestack local imaging: A robust and efficient interpretation tool to control illumination, resolution, and time-lapse properties of reservoirs. 1525–1528

LeCun, Yann, B.Y.H.G. [2015] Deep learning. Nature, 521, 1476–4687.

Leite, E. P., Vidal, A. C., 2011. 3D porosity prediction from seismic inversion and neural networks. Computers & Geosciences, 37(8), 1174-1180.

Manzi, M. S., Gibson, M. A., Hein, K. A., King, N., & Durrheim, R. J. (2012). Application of 3D seismic techniques to evaluate ore resources in the West Wits

Line goldfield and portions of the West Rand goldfield, South Africa. Geophysics, 77(5), WC163-WC171.

Marfurt, K. J., Kirlin, R. L., Farmer, S. L., & Bahorich, M. S. (1998). 3-D seismic attributes using a semblance-based coherency algorithm. Geophysics, 63(4), 1150-1165.

Marfurt, K.J., 2018. Chapter 2. Seismic Attributes and What They Measure. Seismic Attributes as the Framework for Data Integration Throughout the Oilfield Life Cycle. Society of Exploration Geophysicists, 25–149. https://doi.org/10.1190/9781560803522.ch2

McCulloch, W. S., Pitts, W., 1943. A Logical Calculus of the Ideas Immanent in Nervous Activity. The Bulletin of Mathematical Biophysics, 5 (4), 115–33, https://doi.org/10.1007/BF02478259.

Mendes, L. D. C., Correia, U. M., Cunha, O. R., Oliveira, F. M., & Vidal, A. C. (2022). Topological analysis of fault network in naturally fractured reservoirs: A case study from the pre-salt section of the Santos Basin, Brazil. Journal of Structural Geology, 159, 104597.

Mitchell, T. M., 1997. Machine Learning. McGraw-Hill Series in Computer Science. New York: McGraw-Hill.

Montaron, B., Montaron, F., Montaron, R., 2019. A DNN trained to pick faults in seismic data: Implementation and results. International Petroleum Technology Conference 2019, IPTC 2019 26–28. https://doi.org/10.2523/iptc-19116-ms

Nair, Vinod, Hinton, G. E., 2010. Rectified Linear Units Improve Restricted Boltzmann Machines. In Proceedings of the 27th International Conference on International Conference on Machine Learning, 807–14. ICML'10. Madison, WI, USA: Omnipress.

Neto, Eberton & Lupinacci, Wagner & Fernandes, Fábio Júnior & Fatah, Tuany & Dias, Raquel & Freire, Fernando & Lupinacci, Wagner. (2023). A data-driven approach to predict fracture intensity using machine learning for pre-salt carbonate reservoirs.

Nilo, M., Rodrigues, E., Fernandes, F., Teixeira, L. and Lupinacci, W. [2024] A Preconditioning Workflow for Seismic Fault Interpretation Using Deep Learning Applications in the Brazilian Pre-Salt. 2024(1), 1–5.

Oliveira Neto, E. R., Fatah, T. Y. A., Dias, R. M., Freire, A. F. M., & Lupinacci, W. M. (2023). Curvature analysis and its correlation with faults and fractures in presalt carbonates, Santos Basin, Brazil. *Marine and Petroleum Geology*, *158*, 106572.

Otchere, D.A., Tackie-Otoo, B.N., Mohammad, M.A.A., Arbi Ganat, T.O., Kuvakin, N., Miftakhov, R., Efremov, I., Bazanov, A., 2022. Improving seismic fault mapping through data conditioning using a pre-trained deep convolutional neural network: A case study on Groningen field. Journal of Petroleum Science and Engineering 213, 110411. https://doi.org/10.1016/j.petrol.2022.110411

Pedersen, S.I., Randen, T., Sønneland, L., Steen, Ø., 2002. Automatic fault extraction using artificial ants. SEG Technical Program Expanded Abstracts 21, 512–515. https://doi.org/10.1190/1.1817297

Petersohn, E., Morelatto, R., Batista, C. M. A., & Vital, J. C. S. (2021). The Giant Mero oil field: Geological and petrophysical settings of one of the largest pre-salt fields of the Santos Basin, southern Brazil.

Pochet, A., Diniz, P.H.B., Lopes, H., Gattass, M., 2019. Seismic Fault Detection Using Convolutional Neural Networks Trained on Synthetic Poststacked Amplitude Maps. IEEE Geoscience and Remote Sensing Letters 16, 352–356. https://doi.org/10.1109/LGRS.2018.2875836

Qiang, Z., Yasin, Q., Golsanami, N., & Du, Q. (2020). Prediction of reservoir quality from log-core and seismic inversion analysis with an artificial neural network: A case study from the sawan gas field, Pakistan. Energies, 13(2), 486.

Qi, J., Lyu, B., Wu, X., & Marfurt, K. (2020, October). Comparing convolutional neural networking and image processing seismic fault detection methods. In *SEG International Exposition and Annual Meeting* (p. D031S055R006). SEG.

Randen, T., Monsen, E., Signer, C., Abrahamsen, A., Schlaf, J., Sæter, T., & Hansen, J. O. (2000, August). Three-dimensional texture attributes for seismic data analysis. In SEG International Exposition and Annual Meeting (pp. SEG-2000). SEG.

Rich, J. (2008, November). Expanding the applicability of curvature attributes through clarification of ambiguities in derivation and terminology. In SEG International Exposition and Annual Meeting (pp. SEG-2008). SEG.

Robein, E. (2010). Seismic imaging: a review of the techniques, their principles, merits and limitations (EET 4). Earthdoc.

Roberts, A., 2001. Curvature attributes and their application to 3D interpreted horizons. First Break. https://doi.org/10.1046/j.0263-5046.2001.00142.x

Ronneberger, O., Fischer, P., & Brox, T. (2015). U-net: Convolutional networks for biomedical image segmentation. In Medical image computing and computer-assisted intervention–MICCAI 2015: 18th international conference, Munich, Germany, October 5-9, 2015, proceedings, part III 18 (pp. 234-241). Springer International Publishing.

Rumelhart, D., E., Hinton, G. E., Williams, R. J., 1986. Learning Representations by Back-Propagating Errors. Nature: 323 (6088), 533–36. https://doi.org/10.1038/323533a0.

Russell, S. J., Norvig, P., 2021. Artificial Intelligence: A Modern Approach. Fourth edition. Pearson Series in Artificial Intelligence. Hoboken: Pearson.

Sen, S., Kainkaryam, S., Ong, C., Sharma, A., 2020. SaltNet: A production-scale deep learning pipeline for automated salt model building. Leading Edge 39, 195–203. https://doi.org/10.1190/tle39030195.1

Staples, E., Marfurt, K., 2013. Testing Curvature's Impact on Fractures. AAPG Explorer 41147, 42–43.

Tanaka, A. P. B., Borges, J. P. G., de Matos, G. C., Campos, M. T. R., Cunha, B. M., de Souza, R. B., ... & Lima, A. P. M. (2022). Fault-related fracture modeling in a pre-salt lacustrine carbonate reservoir from Santos Basin, offshore Brazil: Predicting preferential fluid flow paths using 3D geological and flow simulation models. Marine and Petroleum Geology, 135, 105392.

Tingdahl, K. M., & De Rooij, M. (2005). Semi-automatic detection of faults in 3D seismic data. Geophysical prospecting, 53(4), 533-542.

Tingdahl, K.M., Bril, A.H., De Groot, P.F., 2001. Improving seismic chimney detection using directional attributes. Journal of Petroleum Science and Engineering 29, 205–211. https://doi.org/10.1016/S0920-4105(01)00090-0

Tingdahl, K.M., De Groot, P.F.M., 2003. Post-stack-dip- and azimuth processing. Journal of Seismic Exploration 12, 113–126.

Trappe, H., Hellmich, C., 2000. Using neural networks to predict porosity thickness from 3D seismic data. First Break, 18(9), https://doi.org/10.1046/j.1365-2397.2000.00091.x.

Vizeu F, Zambrini J, Tertois AL, da Graça e Costa BDA, Fernandes AQ, Canning A (2022) Synthetic seismic data generation for automated AI-based procedures with an example application to high-resolution interpretation. The Leading Edge, 41(6), 392-399.Wu, X. and Hale, D. [2016] 3D seismic image processing for faults. GEOPHYSICS, 81(2), IM1– IM11.

Wang, Z., & AlRegib, G. (2014, May). Fault detection in seismic datasets using hough transform. In 2014 IEEE International Conference on Acoustics, Speech and Signal Processing (ICASSP) (pp. 2372-2376). IEEE.

Wright, V. P., Barnett, A. J., 2015. A. J. An abiotic model for the development of textures in some South Atlantic early Cretaceous lacustrine carbonates. Geological Society, London, Special Publications, 418 (1), 209–219.

Wu, X. and Hale, D. [2016] 3D seismic image processing for faults. GEOPHYSICS, 81(2), IM1– IM11.

Wu, X., Liang, L., Shi, Y. and Fomel, S. [2019] FaultSeg3D: Using synthetic data sets to train an endto-end convolutional neural network for 3D seismic fault segmentation. GEOPHYSICS, 84(3), IM35– IM45.

Y. Ao, W. Lu, P. Xu and B. Jiang, "Seismic Dip Estimation With a Domain Knowledge Constrained Transfer Learning Approach," in IEEE Transactions on Geoscience and Remote Sensing, vol. 60, pp. 1-16, 2022, Art no. 4501216, doi: 10.1109/TGRS.2021.3061438. keywords: {Estimation; Transfer learning; Task analysis; Robustness; Deep learning; Azimuth; Tensors; Convolutional neural network; domain knowledge constraint; seismic dip estimation; transfer learning},

Yang, F., Ma, J., 2019. Deep-learning inversion: A next-generation seismic velocity model building method. Geophysics 84, R583–R599. https://doi.org/10.1190/geo2018-0249.1

You Li, Xinming Wu, Zhenyu Zhu, Jicai Ding, Qingzhen Wang; FaultSeg3D plus: A comprehensive study on evaluating and improving CNN-based seismic fault segmentation. Geophysics 2024; 89 (5): N77–N91. doi: https://doi.org/10.1190/geo2022-0778.1

Zhang, Z., Lei, Y., Mao, X., Li, P., 2019. CNN-FL: An Effective Approach for Localizing Faults using Convolutional Neural Networks. SANER 2019 - Proceedings of the 2019 IEEE 26th International Conference on Software Analysis, Evolution, and Reengineering 445–455. https://doi.org/10.1109/SANER.2019.8668002

Zhao, T., & Mukhopadhyay, P. (2018, October). A fault detection workflow using deep learning and image processing. In SEG International Exposition and Annual Meeting (pp. SEG-2018). SEG.

Zhao, J., Oliveira, M. J. R., Zhao, J., Ren, K., Oliveira, L. C., Carmo, I. O., ... & Deng, Q. (2019, October). Fault activity and its influences on distribution of igneous rocks in Libra block, Santos Basin: Semi-quantitative to quantitative assessment of fault activity based on high-resolution 3D seismic data. In Offshore Technology Conference Brasil (p. D021S016R005). OTC.